An NKX2-1/ERK/WNT feedback loop modulates gastric identity and response to targeted therapy in lung adenocarcinoma

Rediet Zewdu[1,2]; Elnaz Mirzaei Mehrabad[1,3]*; Kelley Ingram[1,4]*; Alex Jones[1,2]; Soledad A. Camolotto[1,2]; Michelle C. Mendoza[1,4]; Benjamin Spike[1,4]; Eric L. Snyder[1,2,4]

1. Huntsman Cancer Institute,

2. Department of Pathology, University of Utah, Salt Lake City, UT 84112

3. School of Computing, University of Utah, Salt Lake City, UT 84112

4. Department of Oncological Sciences, University of Utah, Salt Lake City, UT 84112

*co-second author

Corresponding author: eric.snyder@hci.utah.edu

Key words: Lung adenocarcinoma, Lineage switching, Targeted therapy, NKX2-1, ERK, WNT

ABSTRACT

Cancer cells often undergo lineage switching during their natural progression and in response to therapy. Lung adenocarcinomas (LUADs) exhibit a variety of differentiation states accompanied by dysregulation of lineage-specific transcription factors such as NKX2-1. Loss of NKX2-1 in human and murine LUAD leads to invasive mucinous adenocarcinoma (IMA), a subtype of lung cancer that exhibits pulmonary to gastric transdifferentiation. Human IMAs harbor a distinct spectrum of mutationally activated driver oncogenes compared to LUAD overall, suggesting that the transdifferentiation induced by NKX2-1 loss plays a context-dependent role in LUAD progression. Using genetically engineered mouse models, we find that NKX2-1 is required for optimal $BRAF^{V600E}$ driven lung tumor initiation but is dispensable for growth of established lung tumors. NKX2-1-deficient, $BRAF^{V600E}$ driven tumors morphologically resemble human IMA, have high levels of ERK phosphorylation and exhibit a distinct response to treatment with combined BRAF/MEK inhibitors. Whereas NKX2-1-positive tumor cells enter quiescence when treated with BRAF/MEK inhibitors, residual NKX2-1-negative cells fail to exit the cell cycle in response to the same therapy. Additionally, BRAF/MEK inhibitors induce canonical WNT signaling in NKX2-1-negative lung tumor cells, which is accompanied by cell identity switching within the gastric lineage. Co-inhibition of MAPK and WNT pathways blocked elements of this lineage switch in vitro and interfered with cell cycle changes imposed by MAPK inhibition in vivo. Our data show that there is a complex and reciprocal relationship between lineage specifiers and oncogenic signaling pathways in the regulation of LUAD identity and suggest that lineage switching induced by targeted therapies may confer new therapeutic vulnerabilities.

INTRODUCTION

Lung adenocarcinoma (LUAD), the most common cause of cancer death worldwide, exhibits significant heterogeneity in tumor cell identity and overall differentiation state (Travis et al. 2011). The state of LUAD differentiation correlates closely with prognosis, intrinsic therapeutic sensitivity, and acquisition of drug resistance (Russell et al. 2011; Campos-Parra et al. 2014; Rotow and Bivona 2017). Recent work by our lab and others has shown that the pulmonary lineage specifier NKX2-1/TTF1 is a central regulator of LUAD growth and identity. NKX2-1 is expressed in ~75% of human LUAD, and NKX2-1 negative tumors confer a worse prognosis than NKX2-1-positive tumors (Barletta et al. 2009). The specific role of NKX2-1 in LUAD appears to depend in part on the driver oncogene. The majority of LUADs harbor mutually exclusive mutations in driver oncogenes that signal through the mitogen activated protein kinase (MAPK) pathway, including *EGFR* (14% of cases), *KRAS* (29%) or *BRAF* (7%) (early stage cases, reviewed in (Skoulidis and Heymach 2019)). In this disease, active forms of the RAS family of small GTPases stimulate the RAF/MEK/ERK kinase cascade, which drives proliferation, survival and invasion.

Treatment-naïve *EGFR*-mutant LUADs almost always express NKX2-1, and genetically engineered mouse models (GEMMs) suggest that NKX2-1 is required for optimal growth of *EGFR*-mutant LUAD (Maeda et al. 2012). Intriguingly, case reports suggest NKX2-1 expression can be lost when *EGFR*-mutant LUADs acquire drug resistance during a lineage switch to squamous cell carcinoma (Levin et al. 2015). In contrast to *EGFR* mutant LUAD, NKX2-1 expression is lost in a subset of *KRAS* and *BRAF* mutant tumors (Skoulidis et al. 2015; Zhang et al. 2015). In a *Kras*^{G12D}-mutant LUAD GEMM, *Nkx2-1* deletion enhances tumor growth and causes pulmonary to gastric transdifferentiation (Snyder et al. 2013), which is driven by the transcription factors FoxA1 and FoxA2 (Camolotto et al. 2018). Stochastic NKX2-1 loss has a similar effect on a distinct *KRas*-mutant LUAD GEMM (Maeda et al. 2012) and can promote metastasis when tumors progress in the absence of p53 function (Winslow et al. 2011). *Nkx2-1*-

deficient murine tumors closely resemble invasive mucinous adenocarcinoma (IMA), a subtype of NKX2-1-negative human LUAD that also expresses gastric markers. Human IMAs often harbor mutations in *KRAS* (62% of cases), occasionally *BRAF* (3%, including point mutations and fusions), but rarely *EGFR* (0.6%) (Cha and Shim 2017). These studies suggest that there can be selective pressure for LUAD to either retain or downregulate NKX2-1 expression depending on the specific signaling networks activated by a given driver oncogene.

MAPK signaling is generally considered to drive proliferation and survival in LUAD, and has become a therapeutic target in some contexts. *BRAF*-mutant LUAD exhibit a clinically significant but heterogeneous response to small molecule inhibitors of BRAF and its downstream kinase MEK (Khunger et al. 2018). However, mechanisms underlying heterogeneous responses remain to be identified. MAPK signaling also regulates differentiation state in a variety of tissues, including the stomach, depending on the magnitude and context of its activity (Mendoza et al. 2011; Osaki and Gama 2013). We have previously shown that *Nkx2-1* deletion in $KRAS^{G12D}$ driven LUAD leads to IMA with high levels of MAPK activity, as assessed by levels of active (phosphorylated) ERK1/2 (pERK). In contrast, *Nkx2-1* deletion in alveolar type-2 pneumocytes causes hyperplasia with low levels of pERK (Snyder et al. 2013). IMA and NKX2-1-negative hyperplasia both express some common pan-gastric markers (e.g., HNF4A), demonstrating that loss of NKX2-1 causes pulmonary to gastric transdifferentiation independent of ERK activity. The lesions have a distinct cytologic and architectural properties, suggesting that oncogenic signaling downstream of $KRAS^{G12D}$ modulates the specific identity adopted by an NKX2-1-deficient lung cell.

We have sought to dissect the role of NKX2-1 in *BRaf*-mutant LUAD using a GEMM of this disease. Here, we show that NKX2-1 regulates cellular identity, oncogenic signaling and response to MAPK pathway inhibition in *BRaf*-mutant adenocarcinoma. Our data show that the level of MAPK pathway activity dictates the specific identity adopted by NKX2-1-negative tumor

cells within the gastric lineage. This identity shift is mediated in part by WNT signaling, which is increased after MAPK inhibition in IMA models.

RESULTS

Activation of oncogenic BRAF in the absence of NKX2-1 from alveolar epithelium leads to the development of invasive mucinous adenocarcinoma

To dissect the role of NKX2-1 in mutant BRAF-induced lung adenocarcinoma, we utilized two established mouse strains bearing recombinase-activatable alleles of *BRaf*^{V600E}. In the first mouse model, Cre-sensitive conditional alleles of *BRaf* (*CA/*+) (Dankort et al. 2007), *Trp53* (*f/f*) (Jonkers et al. 2001), *Rosa26*$^{LSL\text{-}tdTomato}$ (Madisen et al. 2010), and *Nkx2-1* (*f/*+ or *f/f*) (Kusakabe et al. 2006) were simultaneously recombined in the mouse lung epithelium upon intratracheal delivery of virus expressing Cre recombinase. Recombination of these alleles simultaneously activates BRAF^{V600E} and tdTomato expression while eliminating p53 and NKX2-1 expression. Mice of the genotype *BRaf*$^{CA/+}$*;Trp53*$^{f/f}$*;Nkx2-1*$^{f/+}$*;Rosa26*$^{LSL\text{-}tdTomato}$ are hereafter referred to as BP mice and mice with the genotype *BRaf*$^{CA/+}$*;Trp53*$^{f/f}$*;Nkx2-1*$^{f/f}$*;Rosa26*$^{LSL\text{-}tdTomato}$ are hereafter referred to as BPN. Initial evaluation of histological (H&E) and molecular features revealed mucin production and gastrointestinal differentiation state in *Nkx2-1*-deficient tumors, including expression of HNF4A, PDX1, Gastrokine 1, Cathepsin E, and Galectin-4 (Fig. 1a and Supplementary Figure 1a). In lung tumors, NKX2-1 is required for sustained expression of surfactant protein genes including *Sftpb* and *Sftpc* (Snyder et al. 2013) as well as the cell surface protein CD36 (Camolotto et al. 2018). Accordingly, immunohistochemical analysis showed that mucinous NKX2-1-negative tumors in BPN mice did not express pro-surfactant proteins B and C as well as CD36 (Supplementary Figure 1b). Overall, NKX2-1-negative tumors in the *BRaf*^{CA} model bore a close resemblance to those previously seen in the KRAS^{G12D} model as well as human IMA (Snyder et al. 2013).

Despite similar morphologic phenotypes, *Nkx2-1* deletion had a profoundly distinct effect on tumor initiation by BRAF^{V600E} in comparison to KRAS^{G12D}. Whereas *Nkx2-1* deletion augmented tumor initiation by KRAS^{G12D} (Snyder et al. 2013), it significantly impaired tumor initiation by BRAF^{V600E}. *Nkx2-1* deletion led to a lower tumor burden 8 weeks after initiation (Fig. 1b) and significantly prolonged overall survival (Fig. 1c). Histopathologic analysis showed that lungs of BP mice harbored predominantly low grade, non-mucinous, NKX2-1-positive tumors, with occasional areas of higher grade nuclei (data not shown). Tumors in BPN mice were predominantly NKX2-1-negative, although a minority of lesions retained NKX2-1 expression, consistent with incomplete recombination of the *Nkx2-1* allele in these lesions. Importantly, many of the NKX2-1-negative tumors progressed to a high grade differentiation state, marked by decreased mucin production and increased nuclear pleomorphism and mitotic rate (Supplementary Fig. 1c). Thus, in this model, loss of NKX2-1 is compatible with tumor progression to a highly malignant state, despite its impairment of tumor initiation.

We have previously shown that loss of lineage specifiers in established tumors can have distinct consequences when compared to loss at the time of tumor initiation (Camolotto et al. 2018). Moreover, models that enable gene manipulation in established tumors are more physiologically relevant to tumor progression than models in which all genetic perturbations are present during tumor initiation. We therefore used a dual recombinase system to assess the role of NKX2-1 in the established BRAF^{V600E} lung adenocarcinoma. Mice harboring FlpO-recombinase sensitive alleles of *BRaf* (*FA/+*) (Shai et al. 2015), *Trp53* (*frt/frt*) (Lee et al. 2012), and *Rosa26* (*FSF-Cre^{ERT2}*) (Schönhuber et al. 2014) were infected with FlpO expressing adenovirus, which enabled recombination of the above alleles and establishment of BRAF^{V600E}-induced lung lesions. After 3 or 6 weeks of tumor growth, *Nkx2-1$^{f/f}$* alleles underwent Cre-based recombination upon injection of mice with tamoxifen. To generate NKX2-1-positive controls, a cohort of mice with the same genotype were injected with vehicle (corn oil). In contrast to vehicle controls, *Nkx2-1* deletion drove transition of established tumors to invasive mucinous

adenocarcinoma (IMA) (Fig. 2a and Supplementary Figure 2a). Collectively, these results and previous work show that *Nkx2-1* deletion promotes a cell lineage switch in LUAD driven by either $KRAS^{G12D}$ or $BRAF^{V600E}$ (Maeda et al. 2012; Snyder et al. 2013).

We next evaluated the effect of NKX2-1 loss on the growth of established $BRAF^{V600E}$ -driven tumors. At early timepoints (3 weeks after tamoxifen), *Nkx2-1* deletion had no significant effect on tumor burden (Fig. 2b). In contrast, *Nkx2-1* deletion in established KRAS-driven tumors (Young et al. 2011) at the same timepoint greatly enhanced tumor burden and lesion number (Fig. 2c). We also found no significant difference in proliferation (assessed by BrdU incorporation) in $BRAF^{V600E}$ -driven tumors after acute loss of *Nkx2-1* (Fig. 2d). Long term analysis revealed no significant difference in survival between corn oil and tamoxifen treated tumor-bearing mice (Fig. 2e). Histopathologic analysis of the survival study revealed that control mice harbored predominantly non-mucinous NKX2-1-positive tumors, whereas tamoxifen-treated mice harbored predominantly NKX2-1-deficient tumors, many of which were high grade, further supporting the notion that NKX2-1 loss is compatible with malignant progression in BRAF-driven lung neoplasia (Supplementary Figure 2b). Finally, we found that knockdown of *Nkx2-1* by targeting short hairpins in the $BRAF^{V600E}$ containing human LUAD cell line, HCC364, does not markedly affect in vitro proliferation (Fig. 2f). Taken together, these data show that loss of NKX2-1 in established $BRAF^{V600E}$ LUAD is tolerated but does not augment tumor growth, in contrast to NKX2-1 loss $KRAS^{G12D}$-driven tumors. This likely explains why *KRAS* mutations are enriched in IMA (relative to LUAD overall), whereas *BRAF* mutations are diminished in frequency, but not excluded altogether like *EGFR* mutations.

Loss of NKX2-1 stimulates MAPK signaling downstream of mutant BRAF

We have previously shown that *Nkx2-1* deletion augments ERK activity in $KRAS^{G12D}$-driven LUAD (Snyder et al. 2013), and feedback inhibition of the MAPK pathway is known to be rate-limiting for the growth of $KRAS^{G12D}$-driven tumors in vivo (Shaw et al. 2007). We therefore

asked whether the *Nkx2-1* deletion also alters MAPK activity in BRAF^{V600E}-driven lung tumors. We initially hypothesized that pERK levels would be similar in BP and BPN tumors, thus explaining the fact that *Nkx2-1* deletion does not augment BRAF^{V600E}-driven lung tumorigenesis. Surprisingly, *Nkx2-1* deletion in both the concomitant and sequential tumor models led to increased MAPK signaling downstream of oncogenic BRAF. Whereas NKX2-1-positive tumors generally exhibited weak, patchy staining for phosphorylated ERK1 and ERK2 (pERK), we observed strong pERK staining in NKX2-1-negative tumors (Fig. 3a and Supplementary Figure 3a). In contrast, phosphorylated levels of MEK1/2 were similar in tumors of both genotypes, suggesting that activation of ERK1/2 in NKX2-1-negative tumors is largely due to regulation downstream of MEK1/2 activity (Fig. 3a). NKX2-1-negative tumors exhibit increased phosphorylation of p90RSK (a direct target of active ERK) and 4E-BP1 and S6 proteins - downstream targets of mTORC1, through which mTORC1 stimulates protein synthesis and cell growth (Roux et al. 2007; Carriere et al. 2011; Mendoza et al. 2011) (Fig. 3a, b and Supplementary Figure 3b). Therefore, NKX2-1-negative tumors exhibit hyperactivation of both MAPK and mTORC1 oncogenic pathways. Importantly, several of these distinguishing features observed in vivo, such as the association between low NKX2-1 and high pERK levels are conserved in vitro in primary tumor organoid cultures from autochthonous BP and BPN tumors (Supplementary Figure 3c). Finally, we performed IHC for pERK on a panel of mucinous primary human lung adenocarcinomas (n=17, see Methods for inclusion criteria). Strong pERK staining was detectable in the majority of mucinous tumors (14/17, Fig. 3c). Among positive cases, seven tumors exhibited diffuse staining (>90% of tumor cells positive), and another seven exhibited partial positivity (20-90% of tumor cells positive). The ERK phosphorylation site is more labile than epitopes recognized by antibodies that detect total protein levels. Therefore, staining patterns likely reflect both biologic heterogeneity and variable processing of clinical specimens. Nevertheless, these data show that the high levels of pERK in IMA mouse models are also found in human IMA.

Response of NKX2-1-positive and NKX2-1-negative tumors to RAF/MEK inhibition

The profound increase in MAPK activity we observed in both in vivo and in vitro models led us to ask whether NKX2-1 status influenced response to MAPK pathway inhibition. To investigate this, we directly compared the effect of RAF/MEK inhibitors on the growth and proliferation of autochthonous BP and BPN lung tumors. Administration of $BRAF^{V600E}$ inhibitor (PLX4720) in combination with MEK inhibitor (PD0325901) effectively suppressed ERK phosphorylation in lung tumors of both genotypes (Fig. 4a). Combined BRAF/MEK inhibition led to a dramatically lower tumor burden in both BP and BPN mice when assessed after two weeks (Fig. 4b) and four weeks (Fig. 4c) of drug treatment. The decrease in tumor burden in BPN mice was greater by two-fold compared to that in BP mice, suggesting that BPN tumors were overall more sensitive to MAPK inhibition. We noted that residual MAPK-inhibited BPN tumors resembled hyperplasia induced by *Nkx2-1* deletion alone with respect to both morphology and low pERK levels (Fig. 4a). NKX2-1-positive, $BRAF^{V600E}$-driven lung tumors have been shown to regress when treated with MEK inhibitor, but regrow rapidly after drug cessation (Trejo et al. 2012). We therefore asked whether drug-treated residual BP and BPN cells retain tumorigenic potential. Histopathologic analysis of BP and BPN tumors treated for four weeks with BRAF/MEK inhibitor followed by drug removal showed that the residual cells of both genotypes readily grew back over the course of 1-4 weeks (Supplementary Figure 4a).

To gain insights into the mechanisms of drug response in each model, we performed transcriptome profiling by bulk and single cell RNA sequencing. Using the Cre-activated *tdTomato* reporter (Madisen et al. 2010) in the $BRaf^{CA}$ model, we enriched tdTomato-positive tumor cells via fluorescence activated cell sorting (FACS). Tumor cells were isolated from mice of both genotypes (BP and BPN) that had been placed on BRAF/MEK inhibitor-diet or control chow for one week.

We first performed Principal Component Analysis (PCA) on bulk RNA sequencing data using the top variable genes. This analysis revealed that the four groups (control and drug treated BP and BPN tumors) could be distinguished at the transcriptomic level. As represented in Fig. 4d, the greatest source of transcriptome diversity was related to deletion of *Nkx2-1* and is reflected by PC1. PC2 was related to MAPK inhibition-imposed transcriptomic changes, which appeared to be greater in BPN tumors than BP tumors. As expected, bulk RNA sequencing demonstrated that representative pulmonary genes including *Sftpb* and *Sftpc* were downregulated in BPN tumors relative to BP tumors regardless of treatment (Supplementary Figure 4b and Supplementary Table 1). In parallel, BPN tumors showed significant upregulation of gastric genes such as *Pdx1* as well as a significant subset of HNF4A-target genes (as revealed by Illumina Correlation Engine) (Supplementary Figure 4c and Supplementary Table 1). Furthermore, *Dusp6*, a transcriptional readout of activated ERK, was significantly downregulated in MAPK-inhibitor treated BP and BPN tumors compared to their respective controls (Supplementary Figure 4d and Supplementary Table 2, 3).

Despite these differences, NKX2-1 targets (e.g. *Sftpc)* were detected at higher levels than expected in sorted BPN tumor cells. This suggested that a subset of these tumor cells may retain NKX2-1 due to incomplete recombination, as we had previously observed by IHC for NKX2-1 (Figure 1 and data not shown). Since the presence of incomplete recombinants limited our ability to comprehensively analyze the transcriptional consequences of NKX2-1 deficiency, we performed additional single cell RNAseq analysis of FACS-sorted BPN tumors (+/- one week of drug treatment) using the 10X Genomics platform. We predicted that this would enable us to circumvent the technical difficulty of resolving complete from incomplete recombinants and also investigate therapy response at the single cell level.

We sequenced 5,065 control and 5,563 drug-treated single BPN cells (Supplementary Figure 4e). Non-tumor cells clustered separately from tumor cells, and their identity was further validated by the expression of well-known stromal markers including *Vim*, *Ptprc*, *Trpm5*, *Pecam1*,

Mgp, *Cd79a*, *Itgam*, *Adgre1*, *Cd3g*, and *Marco*. Filtering for contaminating stromal, endothelial, hematopoietic and low-quality cells reduced the dataset to a total of 6,807 high quality tumor cells (Supplementary Figure 4e). Dimensionality reduction identified eight major tumor clusters (Fig. 4e and Supplementary Table 4). The majority of these cells (70%) fell into three NKX2-1-negative clusters (1-3), which we interpreted to be complete recombinants based on their prevalence, their lack of *Nkx2-1* expression and derepression of multiple gastric markers (Fig. 4f and Supplementary Table 4). This interpretation is further supported by examination of bam files, which did not contain reads mapping to splice junctions of Cre-deleted exons in the *Nkx2-1* gene (Supplemental Figure 4f). Cluster 3 exhibited high expression of *AurkB*, *Plk1*, and other genes that suggest that these cells are in G2/M phase (Fig. 4f and see Fig. 5 for more detail). Cluster 1 and cluster 2 predominantly contain cells from control and drug-treated mice respectively.

In contrast, the remaining cells (30%) exhibited frequent and abundant *Nkx2-1* expression, including splicing from Cre-target exons indicating a failure to recombine (Figure 4f and Supplemental Figure 4f). These cells also frequently expressed the NKX2-1 target *Sftpc* (Fig. 4f). We interpret these cells, which fall into clusters 4-8, to be the incomplete recombinants that we have directly observed microscopically and inferred from bulk RNAseq data. The variable levels of *Nkx2-1* and *Sftpc* in clusters 4-8 (Fig. 4f) suggests that some of these cells represent higher grade tumor cells that stochastically lose NKX2-1 activity and expression, as has been documented in $KRAS^{G12D}$-driven GEMMs (Winslow et al. 2011; Snyder et al. 2013). Additionally, as evidence of tumor dedifferentiation toward a more primitive/high-grade state, we noted the derepression of the embryonic marker, *Hmga2*, in cluster 5 (Supplementary Figure 4g). Similar to cluster 3, cluster 8 exhibited high expression of *AurkB*, *Plk1*, and other genes that suggest that these NKX2-1-positive tumor cells are in G2/M phase. Intriguingly, cluster 8 is comprised almost exclusively of untreated cells, whereas cluster 3 contains a mixture of treated and untreated cells (Fig. 4e, f). This led us to investigate the cell cycle response of BP and BPN tumor cells to drug treatment (Figure 5).

NKX2-1 status influences cell cycle response to RAF/MEK inhibition

The MAPK pathway regulates proliferation by multiple mechanisms, including activating expression of the D-type cyclins, which can drive cells out of quiescence and into the cell division cycle (Lavoie et al. 1996; Tuveson et al. 2004). We therefore evaluated the impact of drug treatment on cell cycle status of BP and BPN lung tumors using IHC for cell cycle markers as well as analysis of RNAseq datasets. We first evaluated drug response by IHC for MCM2, a helicase detectable throughout the cell cycle but not in quiescence (G0). In BP tumors, two weeks of drug treatment led to a significant decline in the percentage of MCM2-positive cells (Fig. 5a and b). Additional IHC analysis showed a decline in the percentage of BP cells positive for BrdU incorporation and phospho-histone H3 (pHH3, M phase marker) (Supplementary Figure 5a-c). Taken together, these data show that drug treatment of BP tumors blocks proliferation and induces cell cycle exit, thereby increasing the proportion of cells in quiescence.

In contrast to BP tumors, drug treatment of BPN tumors led to a paradoxical increase in the percentage of MCM2-positive cells (Fig. 5a and b) despite overt tumor regression (Fig. 4b). In contrast, the percentage of BPN cells positive for BrdU and pHH3 declined to the same extent as BP cells after drug treatment (Supplementary Figure 5a-c). These data suggest that even though BPN cell proliferation is impaired by drug treatment, most residual BPN cells fail to exit the cell cycle and enter quiescence in the absence of MAPK activity.

Analysis of bulk RNA sequencing further demonstrated that BP and BPN tumor cells exhibit a differential cell cycle response to MAPK inhibition. Drug-induced transcriptomic changes were highly distinct between genotypes (Fig. 5c), with only 1/5th of the differentially regulated genes being shared by BP and BPN tumors. Moreover, Pathway analysis (via Illumina Correlation Engine) demonstrated key differences between BP and BPN drug treated lung tumors in the most significant Gene ontology (GO) terms. Specifically, multiple cell cycle-related pathways decline in treated BP tumors, but not in treated BPN tumors, relative to their respective untreated controls

(Fig. 5d and Supplementary Table 5, 6). In contrast, the top GO terms in treated BPN tumors relative to vehicle controls included pathways related extracellular reorganization and cell motility in BPN tumors (Fig. 5e and Supplementary Table 7, 8).

We also modeled transition through the cell cycle in scRNA-seq data using a series of previously reported cell cycle phase signatures (Mizuno et al. 2009) and diffusion mapping (Haghverdi et al. 2015) (Supplementary Figure 5d). Cells with high expression of S-phase or G2/M-phase signatures mapped to successive extremes at the right of the cyclic graph (Fig. 5f), while the majority of cells (>80%) mapped to the left-hand portion corresponding to G0 and G1 signature enrichments (Fig. 5f). Remarkably, these scRNA-seq analyses also revealed NKX2-1 dependent effects of drug treatment on cell cycle status. Treatment of BP cells resulted in their redistribution toward the left hand extreme of the graph, which is most distal from cycling cells and is enriched for the G0 signature, while the distribution of BPN cells was unaffected by treatment (Fig. 5g).

Given the ability of the MAPK pathway to drive cell cycle entry by activation of D-type cyclin expression, we evaluated the expression patterns of *Ccnd1-3* in bulk and single cell RNA sequencing data. Suppression of MAPK activity led to decreased *Ccnd1* transcript levels in both BP and BPN tumors (Supplementary Figure 5e, f) suggesting that the MAPK pathway is a major activator of *Ccnd1* expression in tumors of both genotypes. In contrast, *Ccnd2* mRNA levels were significantly higher in BPN tumors than BP tumors, and drug treatment of BPN tumors led to a further increase in *Ccnd2* levels (Supplementary Figure 5e, f). *Ccnd3* levels were relatively stable across all four conditions (data not shown).

Taken together, these data show that NKX2-1 status has a profound effect on the cell cycle response of $BRAF^{V600E}$-driven lung tumors to targeted therapy. The inability of residual BPN cells to exit the cell cycle suggests that distinct therapeutic strategies will be needed to eliminate BP versus BPN tumor cells after MAPK inhibition. Persistent expression of *Ccnd2* is one possible mechanism by which residual BPN tumor cells might resist cell cycle exit when treated with

RAF/MEK inhibitors. Interestingly, *Ccnd2* expression is activated by other oncogenic signaling pathways, including the WNT pathway in a mouse model of intestinal cancer (Cole et al. 2010).

MAPK pathway regulates identity of NKX2-1-negative mucinous adenocarcinoma within the gastric lineage

Further analysis of gene expression changes in BPN tumors revealed surprising switch-like changes in the expression of lineage markers associated with specific gastric cell types. BPN tumor cells normally express high levels of transcripts that mark surface mucous cells in the stomach, such as *Muc5ac* and *Gkn1*. These surface mucous cell markers declined significantly upon MAPK pathway inhibition (Fig. 6a). In parallel, two of the most highly upregulated genes in drug-treated BPN tumor cells were *Pgc* and *Cym* (Fig. 6a and Supplementary Figure 4d), which encode digestive enzymes normally expressed in chief cells found at the base of the stomach gland (Leushacke et al. 2017; McCracken et al. 2017; Han et al. 2019). Additional markers of murine gastric chief cells including *Gif* and *Clps* were also induced by drug treatment in these tumors (Fig. 6a). *Cym* is expressed predominantly during the neonatal phase of mouse stomach development (Chen et al. 2001; Vallone et al. 2016), suggesting that drug treatment induces an immature chief cell-like phenotype. Drug-treated NKX2-1-negative tumor cells also exhibited induction of several markers of chemosensory tuft cells, including the lineage specifier *Pou2f3* (Kaji and Kaunitz 2017) as well as *Gfi1b* and *Gnat3* (Fig. 6a). We next utilized gene set enrichment analysis (GSEA) to compare the transcriptome of drug treated BPN tumors to published/curated gene expression datasets for gastric epithelial cell types and tuft cells (Haber et al. 2017; Leushacke et al. 2017; Montoro et al. 2018; Ting and von Moltke 2019; Zhang et al. 2019). GSEA showed that signatures of both *Lgr5*-expressing gastric chief cells as well as tuft cells were significantly enriched in MAPK-inhibited BPN cells (Fig. 6b).

A shift in expression of gastric lineage markers was also evident at the single cell level. Our single cell transcriptomics confirmed that gastric surface mucous markers like *Gkn1* and *Tff1*

are downregulated by drug treatment in NKX2-1-negative cells (Fig. 6c). We also found that drug-treated BPN cells have altered their gene expression program to dramatically increase transcript levels of genes associated with chief cells (*Cym*, *Pgc, Pga5*) and tuft cells (*Pou2f3)* (Fig. 6c). *Tff2* transcripts, which mark progenitors located in the isthmus of the normal stomach (Quante et al. 2010), were also increased in drug-treated BPN cells (Fig. 6c).

Finally, we used IHC to evaluate a subset of lineage markers at the protein level in vivo. GKN1 protein (surface mucous marker) was abundant in control BPN tumors, but was depleted in inhibitor-treated BPN tumors (Supplementary Figure 6a). Control BPN tumors were entirely negative for Pepsinogen C, whereas a subset of treated BPN cells were Pepsinogen C-positive (Fig. 6d, upper row). In contrast, a small subset of control BPN tumor cells were POU2F3 positive, and the fraction of positive cells was higher in treated BPN tumors (Fig. 6d, lower row). Both Pepsinogen C and POU2F3-positive cells were found in alveolar hyperplasia induced by *Nkx2-1* deletion, consistent with the possibility that treated BPN tumors regress to a state that resembles these hyperplasias. We also evaluated POU2F3 by IHC in a panel of primary human IMA and found that all tumors examined (n=6) harbored POU2F3-positive cells (Supplementary Figure 6b). Like control BPN tumors, these POU2F3-positive cells were relatively rare in human IMA (~5% or less of tumor cells overall). As expected, all three gastric lineage markers evaluated (GKN1, Pepsinogen C and POU2F3) were undetectable in BP tumors.

We next asked whether regulation of gastric lineage by the MAPK pathway is a general feature of IMA, or limited to $BRAF^{V600E}$-driven tumors. To address this question, we generated organoids from autochthonous IMA models driven by $KRAS^{G12D}$ (KPN) or $BRAF^{V600E}$ (BPN). We treated BPN and KPN organoids with a MEK inhibitor (Cobimetinib) for 3 days and found that this was sufficient to stimulate the expression of chief (*Cym*, *Gif*, *Pgc*) and tuft (*Pou2f3* and *Gfi1b*) cell markers in both KPN and BPN organoid cultures (Supplementary Figure 6c and d). Thus, the MAPK pathway modulates gastric lineage in IMA cells driven by distinct oncogenes (KRAS and BRAF) and in distinct microenvironments (i.e. in vivo and in vitro).

The canonical WNT pathway drives lineage switching and cell cycle response in NKX2-1-negative lung adenocarcinoma treated with RAF/MEK inhibitor

LGR5 marks a subset of normal murine chief cells that can function as facultative stem cells (Leushacke et al. 2017). *Lgr5* is also a canonical WNT target gene, and WNT signaling is thought to promote the regenerative capacity of LGR5-positive chief cells. Given that drug treatment led to an enrichment for the signature of LGR5-positive chief cells in BPN mice, we evaluated our gene expression data to determine whether this was indicative of a general increase in WNT signaling. This was further motivated by observations that WNT signaling can regulate lineage specification and cell cycle entry in the GI tract. WNT/β-catenin signaling plays an essential role in gastric epithelial patterning during embryogenesis, promotes chief cell differentiation (McCracken et al. 2017) and contributes to oncogenesis in a variety of settings (Zhan et al. 2017), including in NKX2-1-positive LUAD GEMMs driven by $BRAF^{V600E}$ (Juan et al. 2014) or $KRAS^{G12D}$ (Tammela et al. 2017). Further, β-catenin activation upon *Apc* deletion in the murine intestinal epithelium specifically upregulates cyclin D2 to augment proliferation and tumorigenesis (Cole et al. 2010).

In our bulk RNA sequencing, multiple transcriptional targets of canonical WNT signaling, including *Axin2*, *Lgr5*, *Wnt11*, *Fzd*, *Fgf9*, *Notum*, *Sox9*, *Lrp1*, *Sox4*, *Znrf3*, *Wnt3A* ('positive regulation of canonical WNT signaling' category on AmiGO, (Carbon et al. 2008)) were significantly activated or, in the case of *Wnt11*, repressed in treated BPN tumors (Fig. 7a). Applying GSEA, we observed an upregulation of a WNT/β-catenin-associated gene signature in drug treated BPN cells relative to control BPNs (Supplementary Figure 7a). Induction of *Axin2* (Jho et al. 2002) and *Lgr5* (Barker et al. 2007) transcripts is considered a hallmark of active WNT/β-catenin signaling, and in our single cell analysis, cells expressing these mRNAs along with other WNT targets emerged with increased frequency in treated BPN tumors (Fig. 7b).

Induction of *Ccnd2* mRNA in treated BPNs (Supplementary Figure 5e and f; Supplementary Figure 7b) is also suggestive of increased WNT/β-catenin activation (Cole et al. 2010). Consistent with our in vivo data, MEK inhibitor stimulated canonical WNT signaling in BPN and KPN organoids as indicated by increased expression of the *Axin2* and *Lgr5* transcripts within the first 24 hours (Supplementary Figure 7c). *Axin2* and *Lgr5* were induced regardless of whether the organoid media composition contained high or low levels of exogenous WNT3A.

Given the established role of WNT signaling in stomach development (McCracken et al. 2017), we asked whether the WNT pathway played a role in the lineage switch induced by MAPK inhibition in IMA. We used two different approaches to modulate WNT signaling in organoid cultures. First, we cultured organoids in 5% conditioned media (L-WRN), which led to a 10 fold reduction in the amount of exogenous WNT3A and R-spondin 3 in the culture media relative to standard conditions (50% L-WRN). Second, we used the small molecule LGK-974, which blocks Porcupine-mediated posttranslational modification of WNT ligands that is required for their secretion and paracrine signaling. Levels of *Axin2* and *Lgr5* were lower in organoids cultured in 5% L-WRN than 50% L-WRN, and treatment with LGK-974 led to a further reduction in these transcripts (Supplementary Figure 7c). This was observed in the presence or absence of MEK inhibition.

We then asked whether WNT signaling was required for lineage switching induced by MEK inhibition. Induction of chief markers (*Cym*, *Pgc*, *Gif*) by MEK inhibitor was partially impaired when WNT signaling was reduced by using 5% L-WRN media alone or in combination with LGK-974 (Fig. 7c). Levels of some chief markers (e.g. *Cym*) were responsive to WNT signaling levels even in the absence of MEK inhibitor. In contrast, tuft cell markers (*Pou2f3* and *Gfi1b*) were largely unaffected by modulation of WNT signaling. These data show that one component of lineage switching (induction of chief cell markers) is partially WNT-dependent, whereas another component (tuft cell marker induction) is largely WNT-independent.

Finally, we asked whether WNT signaling might play a role in failure of BPN tumors to exit the cell cycle after RAF/MEK inhibition. We first correlated known signatures of MEK (Dry et al. 2010) and WNT activity ('positive regulation of canonical WNT signaling' category on AmiGO, (Carbon et al. 2008)) with levels of *Ccnd1* and *Ccnd2* in our single cell data. As expected from bulk data, MEK activity was positively correlated to *Ccnd1* levels across the single cell data set. Conversely, *Ccnd2* levels were inversely correlated to the MEK signature score and positively correlated to the signature for WNT activity (Supplemental Figure 7b).

Given the relationship between WNT activity and *Ccnd2* levels, we asked whether pharmacological WNT inhibition would be sufficient to drive RAF/MEK inhibited BPN cells into quiescence. To address this question, we initiated lung tumors in a cohort of BPN mice and assigned mice to four groups at six weeks after initiation. Four weeks of treatment with RAF/MEK inhibitor led to a significant increase in the percentage of MCM2 positive cells (Fig. 7d), consistent with the effects we observed after 1-2 weeks of treatment (Fig. 5a-b). In contrast, treatment with LGK-974 alone had no effect on MCM2 abundance in BPN tumors. Strikingly, LGK-974 was sufficient to block the induction of MCM2 by RAF/MEK inhibition in BPN tumors, resulting in an MCM2-positive rate similar to controls (Fig. 7d). Thus, induction of WNT signaling after RAF/MEK inhibition acts to prevent residual BPN tumor cells from entering quiescence. Although the addition of short-term LGK-974 to RAF/MEK inhibition was not sufficient to eliminate residual tumor cells entirely (Supplementary Figure 7d), our data show that the biology of residual tumor cells can be manipulated by modulating WNT signaling. These results suggest that longer term manipulation of WNT signaling, or potentially its downstream targets, could be used as a therapeutic strategy to drive residual cells into a permanently non-proliferative state, or even eliminate them altogether.

DISCUSSION

LUAD progression is driven not only by activation of MAPK signaling but also by changes in cellular identity. However, the direct impact of dysregulated MAPK activity on LUAD identity itself remains an unexplored problem in lung cancer. This problem is important not only because of the correlation between cellular identity and intrinsic malignant potential, but also because lineage switching has become an increasingly common mechanism of resistance to therapies targeting the MAPK pathway. A better understanding of this phenomenon would provide new insights into the natural history of LUAD progression as well as the changes in cellular identity that occur as a result of targeted therapy.

Analyses of the histologic spectrum of LUAD in patients and mouse models have identified two cellular differentiation programs that impose barriers to lung tumor progression (Winslow et al. 2011; Snyder et al. 2013; Li et al. 2015; Camolotto et al. 2018). Initially, NKX2-1/FOXA1/2 transcriptional networks maintain a well-differentiated pulmonary identity. We have previously shown that downregulation of NKX2-1 and subsequent relocalization of FOXA1 and FOXA2 to the regulatory elements of gastrointestinal lineage genes allows for loss of surfactant proteins, aberrant upregulation of HNF4A and conversion to gastric cell identity. Loss of both differentiation programs can lead to poorly differentiated tumors containing high levels of HMGA2.

Human IMAs, which are associated with adverse clinical outcomes, most commonly contain *KRAS* mutations (Cha and Shim 2017). *BRAF* mutations are also detectable in IMAs, but at reduced frequency compared to LUAD overall. GEMMs have been valuable in explaining the distinct role of NKX2-1 in LUAD driven by *KRAS* and *EGFR* mutations (Maeda et al. 2012; Snyder et al. 2013). In the present study, we show that NKX2-1 is required for optimal LUAD initiation by $BRAF^{V600E}$, but it is dispensable for growth and progression to high grade states in established tumors. In contrast, loss of NKX2-1 consistently promotes tumorigenesis in $KRAS^{G12D}$-driven GEMMs, regardless of the context. Taken together, these data explain why *KRAS* mutations are enriched in IMA whereas *BRAF* mutations are not. It remains to be determined whether co-mutations can render NKX2-1 loss advantageous (rather than neutral) in *BRAF*-mutant LUADs.

For example, activating codon 201 mutations in *GNAS*, which are predicted to drive cAMP-mediated Protein Kinase A (PKA) activity, occur more frequently in IMA than other LUAD subtypes (Ritterhouse et al. 2017). Although functional studies of GNAS mutations in IMA have not been reported, codon 201 GNAS mutants function as oncogenes in KRAS-driven GEMMs of pancreatic cancer, which expresses some of the same foregut markers as IMA (Taki et al. 2016; Patra et al. 2018). In our RNA sequencing, several mRNAs encoding negative regulators of cAMP-mediated signaling to PKA, including *Prkar2b*, *Rgs7*, and *Adra2a* (Ghavami et al. 2004; Taylor et al. 2008; Garg et al. 2016), were significantly upregulated in BPN cells compared to BP. Interestingly, these transcripts were not elevated in *Nkx2-1* deleted KRAS-driven tumor cells (Camolotto et al. 2018) and decreased cAMP-dependent PKA activity may be one reason why tumor initiation is impaired in BPN tumors.

We have previously shown that the gastric differentiation state of IMA is driven by transcription factors such as FoxA1/2 and HNF4α. Here, we show that MAPK and WNT signaling provide an additional layer of regulation, modulating the specific cell type that IMA cells most closely resemble within the gastric lineage. Our data reveal that high MAPK activity drives a gene expression program characteristic of the surface mucous cells of the stomach. In contrast, low ERK levels, in concert with high WNT activity, activate gene expression signatures associated with other gastric cell types, including LGR5-positive chief cells and tuft cells. Interestingly, hyperactivation of MAPK signaling (via TGF-α mediated activation of EGFR) is observed in Menetrier's disease, a hypertrophic gastropathy characterized by hyperproliferation of isthmus progenitors and the preferential differentiation of these progenitors into surface mucous cells at the expense of parietal and chief cells (Fiske et al. 2009). Blockade of EGFR results in regression of overgrown surface epithelium and restoration of lineage fidelity in progenitors.

Importantly, our results identify crosstalk between the MAPK and WNT pathways in BPN tumors, as suppression of MAPK pathway activates WNT target gene expression within 24 hours.

Crosstalk between these pathways has been observed in other cellular contexts. In the mammalian intestine, reciprocal gradients of WNT and phosphorylated ERK1/2 control the balance between proliferation and differentiation of intestinal stem cells (Kabiri et al. 2018). In one study, reduction of MEK activity via gut-specific ablation of *Ptpn11* impacted the relative levels of TCF4 isoforms, which have differing β-catenin-dependent transactivation capacities (Heuberger et al. 2014). In *Ptpn11* knockout intestine, low MEK activity decreased abundance of TCF4M/S isoforms while favoring the binding of β-catenin to TCF4E variants, which are more efficient drivers of WNT target gene activation. In a second study, treatment of BRAF mutant colorectal cancer cell lines with BRAF inhibitors stimulated WNT pathway through the activation of cytoplasmic focal adhesion kinase (FAK). Activation of FAK was sufficient for β-catenin stabilization and target gene expression (Chen et al. 2018). Yet another study in colorectal cancer models found that MEK inhibitors are potent activators of WNT signaling (Zhan et al. 2019). Multiple MEK inhibitors strongly decreased *AXIN1* transcript and protein levels, perhaps through loss of transactivation by the ERK mediator, EGR1 transcription factor. Decreased expression of AXIN1 led to the disintegration of the β-catenin destruction complex resulting in the accumulation of β-catenin and robust transcription of WNT target genes such as *AXIN2* and *LGR5*. Analogous to what we demonstrate here in BPN lung tumors, the latter two studies documented that suppression of MAPK pathway was accompanied by loss of epithelial differentiation markers and upregulation of intestinal stemness signatures.

Our data also have translational implications for LUAD treatment. *BRAF*-mutant LUADs exhibit a heterogenous response to BRAF/MEK inhibition in clinical trials (Planchard et al. 2016; Planchard et al. 2017). Here we identify NKX2-1 as a determinant of treatment response in a GEMM of this disease. In both NKX2-1-positive and NKX2-1-negative tumors, combined BRAF/MEK inhibition leads to tumor regression, but drug-tolerant cells persist with the potential to relapse. In the absence of NKX2-1, residual tumor cells fail to exit the cell cycle. The different

cell cycle positions of residual BP and BPN tumor cells suggest that different therapeutic approaches will be needed to eradicate these cells. We speculate that agents that inhibit cyclin D2 activity, which is elevated in drug treated BPNs, could be particularly effective against residual tumor cells.

The lineage switch induced by MAPK pathway inhibition in both KRAS and BRAF-driven IMA models is also likely to be relevant to the development of therapeutic interventions for this subtype of LUAD. MAPK inhibition causes IMA cells to undergo an identity shift from a surface mucous cell-like phenotype toward a fate that mimics gastric facultative stem cells as well as tuft cells. These observations support the broader notion that tumor cell plasticity includes the capacity to explore myriad cell states from the developmental repertoire. Lineage switching may be particularly beneficial for tumor cells as diverse lineage programs have distinct therapeutic vulnerabilities. We speculate that cell identity changes within the gastric lineage may render residual IMA cells susceptible to specific therapeutic interventions. For example, short term in vivo WNT inhibition modulated the cell cycle status of IMA cells treated with BRAF/MEK inhibitor, but not control IMA cells (Figure 7). These data are reminiscent of work showing that an identity switch in basal cell carcinoma of the skin confers resistance to inhibition of the Hedgehog pathway while rendering the cells susceptible to blockade of WNT signaling (Biehs et al. 2018; Sanchez-Danes et al. 2018). Thus, in the interest of developing fully effective therapies, these studies call for deep cataloguing of cell states sampled by tumor cells as well as their vulnerabilities.

In summary, this study characterizes the context-dependent role of NKX2-1 in LUAD and identifies novel mechanisms of cell identity regulation and therapeutic response in this disease (Supplementary Figure 7e). These data provide new insights into the complex interplay between lineage specifiers, oncogenic signaling pathways and the susceptibility of lung cancer cells to targeted therapy.

MATERIALS AND METHODS

Mice and tumor initiation

All animal work was done in accordance with a protocol approved by the University of Utah Institutional Animal Care and Use Committee. The following mouse strains were used.

Genotype designation	**Reference**	**Identifiers**	**Additional Information**
BRaf$^{CA/+}$	Dankort et al. 2007 PMID 17299132	MGI:3711771	Dr. Martin McMahon (HCI, Salt Lake City, Utah)
BRaf$^{FA/+}$	Shai et al. 2015 PMID 26001956	MGI:	Dr. Martin McMahon (HCI, Salt Lake City, Utah)
Trp53$^{F/F}$	Jonkers et al. 2001 PMID 11694875	MGI:1931011	Dr. Anton Berns, University of Amsterdam; Jackson Laboratories (Bar Harbor, Maine)
Trp53$^{frt/frt}$	Lee et al. 2012 PMID 22228755	MGI:5306612	Dr. David G Kirsch (Duke University Medical Center, Durham, North Carolina)
KRas$^{LSL-G12D/+}$	Jackson et al. 2001 PMID 11751630	MGI:2429948	Dr. Tyler Jacks (MIT, Cambridge, Massachusetts)
KRas$^{FSF-G12D/+}$	Young et al. 2011 PMID 21512139	MGI:5007794	Dr. Tyler Jacks (MIT, Cambridge, Massachusetts)

Nkx2-1$^{f/f}$	Kusakabe et al. 2006 PMID 16601074	MGI: 3653706	Dr. Shioko Kimura (NCI, NIH, Bethseda, Maryland)
Rosa26 LSL-tdTomato	Madisen et al. 2010 PMID 20023653	MGI: 4436847	Jackson Laboratories (Bar Harbor, Maine)
Rosa26 FSF-Cre^{ERT2}	Schonhuber et al. 2014 PMID 25326799	MGI: 5616874	Dr. Dieter Saur (Technische Universitat Munchen, Munchen, Germany)

Tumors were generated by administering mice with PGK-Cre lentivirus at 5 x 10^3 plaque forming units (pfu)/mouse, Ad5CMVFlpO at 2 x 10^7 pfu/mouse; Ad5CMVCre 2.5 x 10^7 pfu/mouse, Ad5SpcCre 5-8 x 10^8 pfu/mouse or pCDH-CRE 2 x 10^4 pfu/mouse. Adenovirus was obtained from University of Iowa Viral Vector Core.

Rodent Lab Diet (AIN-76A) was formulated with the vemurafenib-related compound PLX4720 at 200 mg/kg (Tsai et al. 2008) and PD0325901 7 mg/kg (Trejo et al. 2012). Drug formulation was by Plexxikon and chow manufacture was by Research Diets. AIN-76A was used as control chow. Mice were maintained on the indicated drug pellets for the indicated time periods. BrdU incorporation was performed by injecting mice at 50 mg/kg (Sigma) intraperitoneally 1 hour prior to necropsy. Mice in survival studies were monitored for lethargy and respiratory distress, at which time animals were euthanized.

Tamoxifen and Doxycycline administration

Tumor-specific activation of CreER^{T2} nuclear activity was achieved by intraperitoneal injection of tamoxifen (Sigma) dissolved in corn oil at a dose of 120 mg/kg. Mice received a total of 6 injections over the course of 9 days. For survival experiments, mice were additionally given pellets supplemented with 500 mg/kg tamoxifen (Envigo).

Cell lines and cell culture

HCC364 cells were cultured in RPMI-1640 medium (Gibco). HEK-293T cells were cultured in DMEM/High Glucose medium (Gibco). L-WRN cells (ATCC) were cultured in DMEM/High Glucose medium containing G418 (Sigma) and Hygromycin (InvivoGen) media. All media contained 10% FBS (Sigma). To eliminate mycoplasma contamination, cell lines were treated with 25 µg/mL Plasmocin (InvivoGen) for 2-3 weeks and to maintain cultures mycoplasma free, media were supplemented with 2.5 µg/mL Plasmocin. Cell line identity was authenticated using STR analysis at the University of Utah DNA Sequencing Core.

Establishing primary lung organoids

8-10 weeks after tumor initiation with PGK-Cre, tumor bearing mice were euthanized and lungs were isolated. Lungs were then minced under sterile conditions and digested at 37°C for 30 mins with continuous agitation in a solution containing the enzymes, Collagen Type I (Thermo Fisher Scientific, at 450 U/ml final); Dispase (Corning, at 5 U/ml); DNaseI (Sigma, at 0.25 mg/ml) and Antibiotic-Antimycotic solution (Gibco). The digested tissue was passed through an 18 or 20-gauge syringe needle. Enzyme reactions were then stopped by addition of cold DMEM/F-12 with 10% FBS and the cell suspension was dispersed through 100 µm, 70 µm and 40 µm series of cell strainers to obtain single cell suspension. Subsequently, cell pellets were treated with erythrocyte lysis buffer (eBioscience). Finally, cell pellets were reconstituted in Advanced DMEM/F-12 (Gibco) supplemented with L-glutamine, 10 mM HEPES, and Antibiotic-Antimycotic. Thereafter, 100,000 tumor cells were mixed with 50 µl of Matrigel (Corning) at 1 to 10 ratio and plated in 24-well plates. For the first week of organoid initiation, Matrigel droplets were overlaid with recombinant organoid medium (Advanced DMEM/F-12 supplemented with 1X B27 (Gibco), 1X N2 (Gibco), 1.25 mM nAcetylcysteine (Sigma), 10 mM Nicotinamide (Sigma), 10 nM Gastrin (Sigma) and containing growth factors (100 ng/ml EGF [Peprotech], 100 ng/ml R-spondin1 [Peprotech], 100 ng/ml Noggin

[Peprotech], 100 ng/ml FGF10 [Peprotech], as well as the ROCK inhibitor Y27632 [R&D Systems] and the TGF-b type I receptor-inhibitor SB431542 [R&D Systems]) as described in (Sato et al. 2009; Barker et al. 2010).

After the initial organoid culture propagation, organoids were switched to 50% L-WRN conditioned media generated as detailed in (Miyoshi and Stappenbeck 2013). Briefly, L-WRN cells (ATCC) seeded and maintained in 10% FBS, DMEM high glucose containing 500 µg/ml G418 (Sigma) and 500 µg/ml Hygromycin (InvivoGen) media until confluency. Once confluent, L-WRN cells were switched to Advanced DMEM/F-12 containing 20% FBS, 2 mM L-glutamine, 100 U/ml penicillin, 0.1 mg/ml streptomycin. Daily, conditioned supernatant medium was collected from L-WRN cultures, filtered through 0.2 µm vacuum filters and saved at -20°C as stock (100%) L-WRN medium. To use for culturing organoids, stock L-WRN was diluted with equal volume Advanced DMEM/F-12 (final concentration 50%). Where specified, stock L-WRN media was diluted with Advanced DMEM/F-12 to a final concentration of 5% while still keeping FBS concentration at 10% as described in (VanDussen et al. 2015). For drug studies, organoid media was supplemented with Cobimetinib (Genentech) and/or LGK-974 (Selleck Chemicals) at indicated concentrations. Drug containing media was refreshed every 48-72hrs.

Lentiviral production

HEK293T cells were transfected with CRE/FLPO-encoding lentiviral vector, d8.9 packaging vector and VSV-G envelope vector mixed with TransIT-293 (Mirus Bio). Virus containing supernatant was collected at 36, 48, 60 and 72 hrs after transfection. Ultracentrifugation at 25,000 r.p.m. for 2 hrs was necessary to concentrate virus for in vivo infection.

Stable knockdown of NKX2-1 was achieved by lentiviral-driven gene silencing using two shRNAs in pLKO.1 vector (*shNkx2-1#1*: TRCN0000020453; *shNkx2-1#2*: TRCN0000415136). short hairpin RNA against GFP was used as control. Lentiviruses were produced and used to

infect HCC364 cells in the presence of 8 µg/ml polybrene for 24 hrs. Puromycin selection for 1 week achieved stable transduction.

Real-time PCR

Total RNA was isolated using TRIzol followed by PureLink RNA Mini Kit (Thermo Fisher Scientific). RNA was treated with RNase-Free DNAse I (Invitrogen) on-column. For low cell numbers (e.g. after FACS), Animal Tissue RNA Purification Kit (Norgen Biotek) was used instead. RNA was converted to cDNA using iScript Reverse Transcription Supermix (BioRad). cDNA was analyzed either by SYBR green real-time PCR with SsoAdvanced Universal SYBR Green Supermix (BioRad) or by Taqman real-time PCR with SsoAdvanced Universal Probes Supermix (BioRad) using a CFX384 Touch Real-Time PCR Detection System (BioRad). Gene expression was calculated relative to *Ppia* (loading control) using the $2^{-(dCt.x-average(dCt.control))}$ method and normalized to the control group for graphing. Primer sequences and TaqMan Assays used in this study are listed below.

Ppia (F), TGTGGTCTTTGGGAAGGTGAA; *Ppia* (R), AAATGGTGATCTTCTTGCTGGT

Muc5ac (F), GTGGTTTGACACTGACTTCCC; *Muc5ac* (R), CTCCTCTCGGTGACAGAGTCT

Ppia Mm02342429_g1; *Muc5ac* Mm01276718_m1; *Gkn1* Mm01183898_m1

Pgc Mm00482488_m1; *Cym* Mm01204823_m1; *GIF* Mm00433596_m1

Pou2f3 Mm00478293_m1; *Gfi1b* Mm00492318_m1; *Lgr5* Mm00438890_m1

Axin2 Mm00443610_m1; *Ccnd1* Mm00432359_m1; *Ccnd2* Mm00438070_m1

Cell viability and growth assay

HCC364 cells were seeded in 96-well plates at a density of 1000 cells per well in 4 technical replicates. For organoids, cells were seeded at a density of 2000 cells per 15 µl Matrigel dome, 3-4 domes per line per time point, each dome in a single well of a 48-well plate. After overnight culture, organoids were treated with different concentrations of the indicated inhibitors

and incubated at 37°C. Cells and organoids were cultured for indicated times. Media was refreshed every 48-72 hours. Subsequently, the relative number of viable cells and organoids was measured by CellTiter-Glo 2.0 Assay or by CellTiter-Glo 3D Cell Viability Assay (Promega), respectively, according to the manufacturer's instructions. Luminescence was then measured by a microplate reader (EnVision 2105 Multimode Plate Reader, PerkinElmer). Replicate values for each experimental group were averaged and all values were normalized to control treatment group for each line. Experiments were repeated at least twice independently.

Immunoblot Analysis

Cells were lysed on ice using RIPA buffer (50 mM HEPES, 140 mM NaCl, 1 mM EDTA, 1% triton X-100, 0.1% sodium deoxycholate and 0.1% SDS) supplemented with protease and phosphatase inhibitor cocktails (Roche). Protein extracts were clarified and concentrations were measured with Pierce Coomassie Plus Protein Assay reagent (Thermo Fisher Scientific). Lysates were then subjected to SDS-PAGE gels (BioRad), and transferred to a Nitrocellulose blots. Membranes were probed with primary antibodies against NKX2-1 (EPR8190-6, Abcam) and β-tubulin (E7, DSHB) and subsequently with DyLight fluorochrome-conjugated secondary antibodies (Thermo Fisher Scientific). Signal was visualized with the Odyssey CLx Imaging System (LI-COR).

Histology and immunohistochemistry

Lung tissues were fixed overnight in 10% neutral buffered formalin, processed through 70% ethanol and embedded in paraffin, sectioned at 4 µm. Staining of hematoxylin and eosin, as well as detection of mucin by Alcian Blue were carried out at the HCI Research Histology Shared Resource. Immunohistochemistry was performed manually as detailed in (Camolotto et al. 2018). The following primary antibodies were used. BrdU (BU1/75, Abcam), Cathepsin E (LS-B523, Lifespan Biosciences), Galectin 4 (AF2128, R and D Systems), Gastrokine 1 (2E5, Abnova),

Histone H3 pSer10 (Abcam), HNF4A (C11F12, CST), MCM2 (ab31159, Abcam), Muc5AC (SPM488, Abnova), NKX2-1 (EP1584Y, Abcam), PDX1 (F109-D12, DSHB), RFP (Rockland Immunochemicals), pERK1/2 (D13.14.4E, CST), p4EBP1 T37/46 (2855, CST), pS6 S235/236 (D57.2.2E, CST), pS6 S240/244 (D68F8, CST), pMEK1/2 S221 (166F8, CST), Pepsinogen C (HPA031718, Sigma), POU2F3 (HPA019652, Sigma). Pictures were taken on a Nikon Eclipse Ni-U microscope with a DS-Ri2 camera and NIS-Elements software. Tumor quantitation was performed on hematoxylin and eosin-stained or IHC-stained slides using NIS-Elements software. All histopathologic analysis was performed by a board-certified anatomic pathologist (E.L.S.).

Primary human tumors

De-identified formalin fixed, paraffin-embedded (FFPE) tumors were obtained from the Intermountain Biorepository, which collects samples in accordance with protocols approved by the Intermountain Healthcare Institutional Review Board. Mucinous tumors were included in the study based on the following criteria: 1. Diagnosis of invasive mucinous adenocarcinoma; OR 2. Diagnosis of mucinous bronchioloalveolar carcinoma (older diagnostic term for IMA); OR 3. Mucinous lung adenocarcinoma with strong morphologic features of IMA, such as abundant intracellular mucin. Colloid adenocarcinomas were excluded, as these are considered to be a discrete subtype of lung cancer.

Fluorescence-activated cell sorting (FACS)

Tumor bearing lungs were isolated in ice-cold PBS. Lungs were enzymatically digested as described above in the procedure for establishing primary organoids. Once single cell suspensions were obtained, cells were reconstituted in phenol red-free DMEM/F-12 with HEPES containing 2% FBS, 2% BSA and DAPI. Cells were sorted using BD FACS Aria for tdTomato-positive and DAPI-negative cells into DMEM/F-12 and 30% serum. After sorting, cells were pelleted and flash frozen or resuspended TRIzol then frozen at -80°C.

Bulk RNA sequencing

Library preparation was performed using the TruSeq Stranded mRNA Library Preparation Kit with poly(A) selection (Illumina). Purified libraries were qualified on an Agilent Technologies 2200 TapeStation using a D1000 ScreenTape assay. The molarity of adapter-modified molecules was defined by quantitative PCR using the Kapa Biosystems Kapa Library Quant Kit. Individual libraries were normalized to 5nM and equal volumes were pooled in preparation for Illumina sequence analysis. Libraries were sequenced on Illumina HiSeq 2500 (50 cycle single-read sequencing v4).

Bulk RNAseq analysis

Adapters in raw FASTQ files containing 50-bp single-end reads were trimmed with cutadapt. QC metrics were generated for each sample with FastQC and Picard's CollectRnaSeqMetrics after aligning reads to genome with STAR (Dobin et al. 2013). QC metrics were summarized by MultiQC. From this QC analysis, one sample (id 14489X13) did not group with other samples in the MultiQC report. it was later confirmed very limited starting material was a contributing factor to its difference from the others. This sample was removed from downstream analysis because the noise in the sample was likely a larger trade-off than the increase in biological replicates for that condition.

Next, Salmon v0.9.1 quantified RNA transcript expression with two steps (Patro et al. 2017); first, the mouse transcriptome downloaded from Gencode (release 26) was indexed using k-mers of length 19 with type 'quasi'; second, Salmon quasi-mapped reads and corrected for sequence-specific bias (see option –seqBias). Salmon-based transcript expression estimates were converted to gene expression estimates with R package tximport (Soneson et al. 2015). Differential gene expression modeling with DESeq2 (Love et al. 2014) and EdgeR (Robinson et al. 2010) evaluated 4 distinct contrasts testing (i) genotype effects within control groups [BP C vs.

BPN C]; (ii) genotype effects within treatment groups [BP Tx vs. BPN Tx]; (iii) treatment effects within BP genotype [BP C vs. BP Tx]; (iv) treatment effects within BPN genotype [BPN C vs. BPN Tx]. Prior to fitting a single-factor DESeq2 regression (4 factor levels: BP C, BPN C, BP Tx, BPN Tx), genes were filtered if there were less than 5 total counts across all samples. PCA was done on the top 500 most variable genes subject to a regularized log transform to confirm within-group variation was similar. A Wald test was applied to the fitted model for each of the 4 contrasts specified above, where the null hypothesis was gene expression differences was less than or equal to log2(2) fold change in absolute value and the alternative hypothesis was that differences exceed log2(2). Significance of gene-wise differences was controlled by a false discovery rate of 10% (Benjamini and Hochberg 1995).

Differential gene expression modeling with EdgeR for volcano plots used package edgeR_3.24.3 with ggplot2_3.1.1. Significance of gene-wise differences was calculated by tag-wise exact test. WNT signaling genes were delineated in the bulk sequencing matrix using AmiGO pathway annotations (http://amigo.geneontology.org) for “Wnt Signaling” (Carbon et al. 2008). WNT genes were restricted to those annotated for *Mus musculus* with direct experimental evidence. The most differentially expressed genes between treated and untreated sample groups (Bonferonni corrected Student’s t-test) were thresholded at >2 fold change between means of treated and untreated samples.

Gene set enrichment analysis (GSEA) was carried out on bulk data (and single cell data (below)) by comparing gene expression profiles with archived gene sets from Hallmarks [ftp.broadinstitute.org://pub/gsea/gene_sets/h.all.v7.0.symbols.gmt] and Oncogenic signatures [ftp.broadinstitute.org://pub/gsea/gene_sets/c6.all.v7.0.symbols.gmt] as well as with the cell type specific genes sets described in (Haber et al. 2017; Leushacke et al. 2017; Montoro et al. 2018; Zhang et al. 2019).

Single-cell RNA sequencing

All protocols to generate scRNA-seq data on 10x Genomics Chromium platform including library prep, instrument and sequencing setting can be found on: https://support.10xgenomics.com/single-cell-gene-expression

The Chromium Single Cell Gene Expression Solution with 3' chemistry, version 3 (PN-1000075) was used to barcode individual cells with 16 bp 10x Barcode and to tag cell specific transcript molecules with 10 bp Unique Molecular Identifier (UMI) according to the manufacturer's instructions. The following protocol was performed at High-Throughput Genomics Shared Resources at Huntsman Cancer Institute, University of Utah. First, FACS sorted single cell suspensions of tdTomato-positive lung tumors were resuspended in phosphate buffered saline with 0.04% bovine serum albumin. The cell suspension was filtered through 40 micron cell strainer. Viability and cell count were assessed on Countess I (Thermo Scientific). Equilibrium to targeted cell recovery of 6,000 cells, along with 10x Gel Beads and reverse transcription reagents were loaded to Chromium Single Cell A (PN-120236) to form Gel Beads-in emulsions (GEMs), the nano-droplets. Within individual GEMs, cDNA generated from captured and barcoded mRNA was synthesized by reverse transcription at the setting of 53°C for 45 min followed by 85°C for 5 min. Subsequent A tailing, end repair, adaptor ligation and sample indexing were performed in bulk according to the manufacturer's instructions. The resulting barcoding libraries were qualified on Agilent D1000 ScreenTape on Agilent Technology 2200 TapeStation system and quantified by quantification PCR using KAPA Biosystems Library Quantification Kit for Illumine Platforms (KK4842). Multiple libraries were then normalized and sequenced on NovaSeq 6000 with 2x150 PE mode.

Single-cell RNAseq analysis

Demultiplexing and data alignment: Single cell RNAseq data were demultiplexed with 10x cellranger mkfastq version 3.1.0 to create fastq files with the I1 sample index, R1 cell barcode+UMI and R2 sequence. Reads were aligned to the mouse genome (mm10 with custom

tdTomato reference) and feature counts were generated using cellranger count 3.1.0 with expected-cells set to 6000 per library. QC reporting, clustering, dimension reduction, and differential gene expression analysis were performed in 10x Genomics' Cell Loupe Browser (v3.1.1). For the BPN control sample, we captured 5,065 cells and obtained 46,894 mean reads per cell; 3,544 median genes per cell. For the BPN treated sample, we captured 5,563 cells and obtained 37,488 mean reads per cell; 2,771 median genes per cell. For further details of the primary Cell Ranger data processing, see https:// support.10xgenomics.com/single-cell-gene-expression/software/pipelines/latest/algorithms/.

Visualization and expression analysis: Single cell expression data was analyzed using Seurat (3.1.0) (Butler et al. 2018; Stuart et al. 2019) and visualized in Loupe browser (3.1.1). Alternatively, single cell data was processed mostly in R (3.5.1). Cells with unique feature counts over 7,500 or less than 200 and more than 20% mitochondrial counts have been filtered out. For visualization, the umap-learn package, from Seurat (McInnes et al. 2018), was used to reduce the dimensionality of the data.

Clustering: The Seurat package clustering method was used to designate cluster membership of single cell transcriptomics profiles. Seurat clustering is heavily inspired by (Levine et al. 2015; Xu and Su 2015), which has 2 steps in the first step, the findNeighbors function is employed to embed single cell profiles in a K-nearest neighbor (KNN) graph based euclidean distance in a (20 PCs) PCA space. Following by refining the edge weights based on jaccard similarity (https://satijalab.org/seurat/v3.0/pbmc3k_tutorial.html). In the second step, the FindClusters function employs Louvain algorithm modularity optimization techniques to iteratively group cells together (https://satijalab.org/seurat/v3.0/pbmc3k_tutorial.html).

Stromal cell designations: Clusters of cells sharing highly similar positions in dimensionality reduced UMAP-space were examined for differential expression using Loupe browser's built in differential expression calculator, and genes showing significant cluster specific expression were screened manually against the literature for markers of known cell types. Those

clusters representing minority populations that were highly distinct in Umap-space from the bulk of cells in the analysis and which bear distinctive expression of stromal marker genes were considered as stromal contaminants and removed from subsequent, tumor-specific Umap data visualization and cluster specific gene expression level analysis.

Cell cycle phase modeling: Cell cycle phase was modeled by determining mean expression per cell of previously published, cell cycle phase signatures from bulk data (Mizuno et al. 2009). A matrix of these values was then graphed as a diffusion map using the Destiny package (Angerer et al. 2015) in R. A coherent cell cycle loop through three dimensional space using the first three diffusion components was projected onto two dimensions using an heuristic arithmetic, diffusion component combination. To this graph a principal curve was fit using Princurve (Hastie and Stuetzle 1989) and tangents for each point (lambdas) were used as cellular positions along a trajectory designated as Q-depth based on the position of g0-signature enriched cells (an indicator related to quiescence) at the extreme distal to cells enriched in g1 signatures or the S and G2/M signatures.

MEK activation signature and WNT signature expression: Average expression of an 18 gene signature from Dry et al. (Dry et al. 2010) was determined per cell across the single cell data set to model MEK activation state. Similarly, average expression of the GO ontology category (AmiGO) for 'positive regulation of canonical WNT signaling' (Carbon et al. 2008) was used to model overall WNT activation state.

Recombination fidelity: Cluster specific BAM files were parsed from the concatenated scRNA-Seq BAM files using subset-bam tool (https://github.com/10XGenomics/subset-bam). The presence of select splice junctions was visualized using IGV (version 2.7.2) (Robinson et al. 2011) against mouse genome version (mm10).

Statistics

p-Values were calculated using the unpaired two-tailed t-test. RNAseq statistics are described above.

DATA AVAILABILITY

All sequencing data generated in this study are available at Gene Expression Omnibus (GEO: GSE145152).

ACKNOWLEDGEMENTS

We are grateful to members of the Snyder lab for suggestions and comments. We acknowledge Plexxikon for providing PLX4720 and PD0325901; Research Diets for compounding. We thank Brian Dalley and Opal Allen for sequencing expertise, Chris Conley for RNA sequencing data analysis expertise, and James Marvin for FACS expertise. Work in the flow cytometry core was supported by the National Center for Research Resources of the National Institutes of Health under Award Number 1S20RR026802-1. Research reported in this publication utilized shared resources (including Flow Cytometry, High Throughput Genomics, Bioinformatics, and Biorepository and Molecular Pathology) at the University of Utah and was supported by Huntsman Cancer Foundation and the National Cancer Institute of the National Institutes of Health under Award Number P30CA042014. The content is solely the responsibility of the authors and does not necessarily represent the official views of the NIH. E.L.S. was supported in part by a Career Award for Medical Scientists from the Burroughs Wellcome Fund, a V Scholar Award, the NIH (R01CA212415), a Pilot Project Award from the Lung Cancer Center of the Huntsman Cancer Institute, and institutional funds (Department of Pathology and Huntsman Cancer Institute, University of Utah). M.C.M and K.I. were supported by an American Lung Association Research Grant, V Foundation Fellowship, and R21CA215891 to M.C.M.

AUTHOR CONTRIBUTIONS

Conception and design: ELS, RZ; Acquisition of data: RZ, ELS; Computational analysis: BS, EMM; Technical/material support: KI, SAC, AJ, MCM; Writing, review of manuscript: all; Study supervision: ELS

CONFLICTS OF INTEREST/ DISCLOSURE

None.

REFERENCES

Angerer P, Haghverdi L, Büttner M, Theis FJ, Marr C, Buettner F. 2015. destiny: diffusion maps for large-scale single-cell data in R. *Bioinformatics* **32**: 1241-1243.

Barker N, Huch M, Kujala P, van de Wetering M, Snippert HJ, van Es JH, Sato T, Stange DE, Begthel H, van den Born M. 2010. Lgr5+ ve stem cells drive self-renewal in the stomach and build long-lived gastric units in vitro. *Cell stem cell* **6**: 25-36.

Barker N, Van Es JH, Kuipers J, Kujala P, Van Den Born M, Cozijnsen M, Haegebarth A, Korving J, Begthel H, Peters PJ. 2007. Identification of stem cells in small intestine and colon by marker gene Lgr5. *Nature* **449**: 1003.

Barletta JA, Perner S, Iafrate AJ, Yeap BY, Weir BA, Johnson LA, Johnson BE, Meyerson M, Rubin MA, Travis WD et al. 2009. Clinical significance of TTF-1 protein expression and TTF-1 gene amplification in lung adenocarcinoma. *J Cell Mol Med* **13**: 1977-1986.

Benjamini Y, Hochberg Y. 1995. Controlling the false discovery rate: a practical and powerful approach to multiple testing. *Journal of the Royal statistical society: series B (Methodological)* **57**: 289-300.

Biehs B, Dijkgraaf GJP, Piskol R, Alicke B, Boumahdi S, Peale F, Gould SE, de Sauvage FJ. 2018. A cell identity switch allows residual BCC to survive Hedgehog pathway inhibition. *Nature* **562**: 429-433.

Butler A, Hoffman P, Smibert P, Papalexi E, Satija R. 2018. Integrating single-cell transcriptomic data across different conditions, technologies, and species. *Nature biotechnology* **36**: 411.

Camolotto SA, Pattabiraman S, Mosbruger TL, Jones A, Belova VK, Orstad G, Streiff M, Salmond L, Stubben C, Kaestner KH. 2018. FoxA1 and FoxA2 drive gastric differentiation and suppress squamous identity in NKX2-1-negative lung cancer. *Elife* **7**: e38579.

Campos-Parra AD, Aviles A, Contreras-Reyes S, Rojas-Marin CE, Sanchez-Reyes R, Borbolla-Escoboza RJ, Arrieta O. 2014. Relevance of the novel IASLC/ATS/ERS classification of lung adenocarcinoma in advanced disease. *Eur Respir J* **43**: 1439-1447.

Carbon S, Ireland A, Mungall CJ, Shu S, Marshall B, Lewis S, Hub A, Group WPW. 2008. AmiGO: online access to ontology and annotation data. *Bioinformatics* **25**: 288-289.

Carriere A, Romeo Y, Acosta-Jaquez HA, Moreau J, Bonneil E, Thibault P, Fingar DC, Roux PP. 2011. ERK1/2 phosphorylate Raptor to promote Ras-dependent activation of mTOR complex 1 (mTORC1). *Journal of Biological Chemistry* **286**: 567-577.

Cha YJ, Shim HS. 2017. Biology of invasive mucinous adenocarcinoma of the lung. *Translational lung cancer research* **6**: 508.

Chen G, Gao C, Gao X, Zhang DH, Kuan S-F, Burns TF, Hu J. 2018. Wnt/β-catenin pathway activation mediates adaptive resistance to BRAF inhibition in colorectal cancer. *Molecular cancer therapeutics* **17**: 806-813.

Chen X, Rosenfeld CS, Roberts RM, Green JA. 2001. An aspartic proteinase expressed in the yolk sac and neonatal stomach of the mouse. *Biology of reproduction* **65**: 1092-1101.

Cole AM, Myant K, Reed KR, Ridgway RA, Athineos D, Van den Brink GR, Muncan V, Clevers H, Clarke AR, Sicinski P. 2010. Cyclin D2–cyclin-dependent kinase 4/6 is required for efficient proliferation and tumorigenesis following Apc loss. *Cancer research* **70**: 8149-8158.

Dankort D, Filenova E, Collado M, Serrano M, Jones K, McMahon M. 2007. A new mouse model to explore the initiation, progression, and therapy of BRAFV600E-induced lung tumors. *Genes & development* **21**: 379-384.

Dobin A, Davis CA, Schlesinger F, Drenkow J, Zaleski C, Jha S, Batut P, Chaisson M, Gingeras TR. 2013. STAR: ultrafast universal RNA-seq aligner. *Bioinformatics* **29**: 15-21.

Dry JR, Pavey S, Pratilas CA, Harbron C, Runswick S, Hodgson D, Chresta C, McCormack R, Byrne N, Cockerill M. 2010. Transcriptional pathway signatures predict MEK addiction and response to selumetinib (AZD6244). *Cancer research* **70**: 2264-2273.

Fiske WH, Tanksley J, Nam KT, Goldenring JR, Slebos RJ, Liebler DC, Abtahi AM, La Fleur B, Ayers GD, Lind CD. 2009. Efficacy of cetuximab in the treatment of Menetrier's disease. *Science translational medicine* **1**: 8ra18-18ra18.

Garg A, Sankella S, Xing C, Agarwal AK. 2016. Whole-exome sequencing identifies ADRA2A mutation in atypical familial partial lipodystrophy. *JCI Insight* **1**.

Ghavami A, Hunt RA, Olsen MA, Zhang J, Smith DL, Kalgaonkar S, Rahman Z, Young KH. 2004. Differential effects of regulator of G protein signaling (RGS) proteins on serotonin 5-HT1A, 5-HT2A, and dopamine D2 receptor-mediated signaling and adenylyl cyclase activity. *Cell Signal* **16**: 711-721.

Haber AL, Biton M, Rogel N, Herbst RH, Shekhar K, Smillie C, Burgin G, Delorey TM, Howitt MR, Katz Y. 2017. A single-cell survey of the small intestinal epithelium. *Nature* **551**: 333.

Haghverdi L, Buettner F, Theis FJ. 2015. Diffusion maps for high-dimensional single-cell analysis of differentiation data. *Bioinformatics* **31**: 2989-2998.

Han S, Fink J, Jörg DJ, Lee E, Yum MK, Chatzeli L, Merker SR, Josserand M, Trendafilova T, Andersson-Rolf A. 2019. Defining the identity and dynamics of adult gastric isthmus stem cells. *Cell stem cell*.

Hastie T, Stuetzle W. 1989. Source: Journal of the American Statistical Association, Vol. 84, No. 406,(Jun., 1989), pp. 502. *Journal of the American Statistical Association* **84**: 502.

Heuberger J, Kosel F, Qi J, Grossmann KS, Rajewsky K, Birchmeier W. 2014. Shp2/MAPK signaling controls goblet/paneth cell fate decisions in the intestine. *Proceedings of the National Academy of Sciences* **111**: 3472-3477.

Jho E-h, Zhang T, Domon C, Joo C-K, Freund J-N, Costantini F. 2002. Wnt/β-catenin/Tcf signaling induces the transcription of Axin2, a negative regulator of the signaling pathway. *Molecular and cellular biology* **22**: 1172-1183.

Jonkers J, Meuwissen R, van der Gulden H, Peterse H, van der Valk M, Berns A. 2001. Synergistic tumor suppressor activity of BRCA2 and p53 in a conditional mouse model for breast cancer. *Nature genetics* **29**: 418.

Juan J, Muraguchi T, Iezza G, Sears RC, McMahon M. 2014. Diminished WNT -> beta-catenin -> c-MYC signaling is a barrier for malignant progression of BRAFV600E-induced lung tumors. *Genes Dev* **28**: 561-575.

Kabiri Z, Greicius G, Zaribafzadeh H, Hemmerich A, Counter CM, Virshup DM. 2018. Wnt signaling suppresses MAPK-driven proliferation of intestinal stem cells. *Journal of Clinical Investigation* **128**: 3806-3812.

Kaji I, Kaunitz JD. 2017. Luminal chemosensing in the gastroduodenal mucosa. *Current opinion in gastroenterology* **33**: 439-445.

Khunger A, Khunger M, Velcheti V. 2018. Dabrafenib in combination with trametinib in the treatment of patients with BRAF V600-positive advanced or metastatic non-small cell lung cancer: clinical evidence and experience. *Therapeutic advances in respiratory disease* **12**: 1753466618767611.

Kusakabe T, Kawaguchi A, Hoshi N, Kawaguchi R, Hoshi S, Kimura S. 2006. Thyroid-specific enhancer-binding protein/NKX2. 1 is required for the maintenance of ordered architecture and function of the differentiated thyroid. *Molecular endocrinology* **20**: 1796-1809.

Lavoie JN, L'Allemain G, Brunet A, Muller R, Pouyssegur J. 1996. Cyclin D1 expression is regulated positively by the p42/p44MAPK and negatively by the p38/HOGMAPK pathway. *J Biol Chem* **271**: 20608-20616.

Lee C-L, Moding EJ, Huang X, Li Y, Woodlief LZ, Rodrigues RC, Ma Y, Kirsch DG. 2012. Generation of primary tumors with Flp recombinase in FRT-flanked p53 mice. *Disease models & mechanisms* **5**: 397-402.

Leushacke M, Tan SH, Wong A, Swathi Y, Hajamohideen A, Tan LT, Goh J, Wong E, Denil SL, Murakami K. 2017. Lgr5-expressing chief cells drive epithelial regeneration and cancer in the oxyntic stomach. *Nature cell biology* **19**: 774.

Levin PA, Mayer M, Hoskin S, Sailors J, Oliver DH, Gerber DE. 2015. Histologic Transformation from Adenocarcinoma to Squamous Cell Carcinoma as a Mechanism of Resistance to EGFR Inhibition. *J Thorac Oncol* **10**: e86-e88.

Levine JH, Simonds EF, Bendall SC, Davis KL, El-ad DA, Tadmor MD, Litvin O, Fienberg HG, Jager A, Zunder ER. 2015. Data-driven phenotypic dissection of AML reveals progenitor-like cells that correlate with prognosis. *Cell* **162**: 184-197.

Li CM, Gocheva V, Oudin MJ, Bhutkar A, Wang SY, Date SR, Ng SR, Whittaker CA, Bronson RT, Snyder EL et al. 2015. Foxa2 and Cdx2 cooperate with Nkx2-1 to inhibit lung adenocarcinoma metastasis. *Genes Dev* **29**: 1850-1862.

Love MI, Huber W, Anders S. 2014. Moderated estimation of fold change and dispersion for RNA-seq data with DESeq2. *Genome biology* **15**: 550.

Madisen L, Zwingman TA, Sunkin SM, Oh SW, Zariwala HA, Gu H, Ng LL, Palmiter RD, Hawrylycz MJ, Jones AR. 2010. A robust and high-throughput Cre reporting and characterization system for the whole mouse brain. *Nature neuroscience* **13**: 133.

Maeda Y, Tsuchiya T, Hao H, Tompkins DH, Xu Y, Mucenski ML, Du L, Keiser AR, Fukazawa T, Naomoto Y. 2012. Kras G12D and Nkx2-1 haploinsufficiency induce mucinous adenocarcinoma of the lung. *The Journal of clinical investigation* **122**: 4388-4400.

McCracken KW, Aihara E, Martin B, Crawford CM, Broda T, Treguier J, Zhang X, Shannon JM, Montrose MH, Wells JM. 2017. Wnt/β-catenin promotes gastric fundus specification in mice and humans. *Nature* **541**: 182.

McInnes L, Healy J, Melville J. 2018. Umap: Uniform manifold approximation and projection for dimension reduction. *arXiv preprint arXiv:180203426*.

Mendoza MC, Er EE, Blenis J. 2011. The Ras-ERK and PI3K-mTOR pathways: cross-talk and compensation. *Trends in biochemical sciences* **36**: 320-328.

Miyoshi H, Stappenbeck TS. 2013. In vitro expansion and genetic modification of gastrointestinal stem cells in spheroid culture. *Nature protocols* **8**: 2471.

Mizuno H, Nakanishi Y, Ishii N, Sarai A, Kitada K. 2009. A signature-based method for indexing cell cycle phase distribution from microarray profiles. *BMC genomics* **10**: 137.

Montoro DT, Haber AL, Biton M, Vinarsky V, Lin B, Birket SE, Yuan F, Chen S, Leung HM, Villoria J. 2018. A revised airway epithelial hierarchy includes CFTR-expressing ionocytes. *Nature* **560**: 319.

Osaki L, Gama P. 2013. MAPKs and signal transduction in the control of gastrointestinal epithelial cell proliferation and differentiation. *International journal of molecular sciences* **14**: 10143-10161.

Patra KC, Kato Y, Mizukami Y, Widholz S, Boukhali M, Revenco I, Grossman EA, Ji F, Sadreyev RI, Liss AS et al. 2018. Mutant GNAS drives pancreatic tumourigenesis by inducing PKA-mediated SIK suppression and reprogramming lipid metabolism. *Nature cell biology* **20**: 811-822.

Patro R, Duggal G, Love MI, Irizarry RA, Kingsford C. 2017. Salmon provides fast and bias-aware quantification of transcript expression. *Nature methods* **14**: 417.

Planchard D, Besse B, Groen HJ, Souquet P-J, Quoix E, Baik CS, Barlesi F, Kim TM, Mazieres J, Novello S. 2016. Dabrafenib plus trametinib in patients with previously treated BRAFV600E-mutant metastatic non-small cell lung cancer: an open-label, multicentre phase 2 trial. *The Lancet Oncology* **17**: 984-993.

Planchard D, Smit EF, Groen HJ, Mazieres J, Besse B, Helland Å, Giannone V, D'Amelio Jr AM, Zhang P, Mookerjee B. 2017. Dabrafenib plus trametinib in patients with previously untreated BRAFV600E-mutant metastatic non-small-cell lung cancer: an open-label, phase 2 trial. *The Lancet Oncology* **18**: 1307-1316.

Quante M, Marrache F, Goldenring JR, Wang TC. 2010. TFF2 mRNA transcript expression marks a gland progenitor cell of the gastric oxyntic mucosa. *Gastroenterology* **139**: 2018-2027. e2012.

Ritterhouse LL, Vivero M, Mino-Kenudson M, Sholl LM, Iafrate AJ, Nardi V, Dong F. 2017. GNAS mutations in primary mucinous and non-mucinous lung adenocarcinomas. *Mod Pathol* **30**: 1720-1727.

Robinson JT, Thorvaldsdóttir H, Winckler W, Guttman M, Lander ES, Getz G, Mesirov JP. 2011. Integrative genomics viewer. *Nature biotechnology* **29**: 24.

Robinson MD, McCarthy DJ, Smyth GK. 2010. edgeR: a Bioconductor package for differential expression analysis of digital gene expression data. *Bioinformatics* **26**: 139-140.

Rotow J, Bivona TG. 2017. Understanding and targeting resistance mechanisms in NSCLC. *Nature reviews Cancer* **17**: 637-658.

Roux PP, Shahbazian D, Vu H, Holz MK, Cohen MS, Taunton J, Sonenberg N, Blenis J. 2007. RAS/ERK signaling promotes site-specific ribosomal protein S6 phosphorylation via RSK and stimulates cap-dependent translation. *Journal of Biological Chemistry* **282**: 14056-14064.

Russell PA, Wainer Z, Wright GM, Daniels M, Conron M, Williams RA. 2011. Does lung adenocarcinoma subtype predict patient survival?: A clinicopathologic study based on the new International Association for the Study of Lung Cancer/American Thoracic Society/European Respiratory Society international multidisciplinary lung adenocarcinoma classification. *J Thorac Oncol* **6**: 1496-1504.

Sanchez-Danes A, Larsimont JC, Liagre M, Munoz-Couselo E, Lapouge G, Brisebarre A, Dubois C, Suppa M, Sukumaran V, Del Marmol V et al. 2018. A slow-cycling LGR5 tumour population mediates basal cell carcinoma relapse after therapy. *Nature* **562**: 434-438.

Sato T, Vries RG, Snippert HJ, Van De Wetering M, Barker N, Stange DE, Van Es JH, Abo A, Kujala P, Peters PJ. 2009. Single Lgr5 stem cells build crypt–villus structures in vitro without a mesenchymal niche. *Nature* **459**: 262.

Schönhuber N, Seidler B, Schuck K, Veltkamp C, Schachtler C, Zukowska M, Eser S, Feyerabend TB, Paul MC, Eser P. 2014. A next-generation dual-recombinase system for time-and host-specific targeting of pancreatic cancer. *Nature medicine* **20**: 1340.

Shai A, Dankort D, Juan J, Green S, McMahon M. 2015. TP53 silencing bypasses growth arrest of BRAFV600E-induced lung tumor cells in a two-switch model of lung tumorigenesis. *Cancer research* **75**: 3167-3180.

Shaw AT, Meissner A, Dowdle JA, Crowley D, Magendantz M, Ouyang C, Parisi T, Rajagopal J, Blank LJ, Bronson RT et al. 2007. Sprouty-2 regulates oncogenic K-ras in lung development and tumorigenesis. *Genes Dev* **21**: 694-707.

Skoulidis F, Byers LA, Diao L, Papadimitrakopoulou VA, Tong P, Izzo J, Behrens C, Kadara H, Parra ER, Canales JR et al. 2015. Co-occurring genomic alterations define major subsets

of KRAS-mutant lung adenocarcinoma with distinct biology, immune profiles, and therapeutic vulnerabilities. *Cancer Discov* **5**: 860-877.

Skoulidis F, Heymach JV. 2019. Co-occurring genomic alterations in non-small-cell lung cancer biology and therapy. *Nat Rev Cancer* **19**: 495-509.

Snyder EL, Watanabe H, Magendantz M, Hoersch S, Chen TA, Wang DG, Crowley D, Whittaker CA, Meyerson M, Kimura S. 2013. Nkx2-1 represses a latent gastric differentiation program in lung adenocarcinoma. *Molecular cell* **50**: 185-199.

Soneson C, Love MI, Robinson MD. 2015. Differential analyses for RNA-seq: transcript-level estimates improve gene-level inferences. *F1000Research* **4**.

Stuart T, Butler A, Hoffman P, Hafemeister C, Papalexi E, Mauck III WM, Hao Y, Stoeckius M, Smibert P, Satija R. 2019. Comprehensive Integration of Single-Cell Data. *Cell*.

Taki K, Ohmuraya M, Tanji E, Komatsu H, Hashimoto D, Semba K, Araki K, Kawaguchi Y, Baba H, Furukawa T. 2016. GNAS(R201H) and Kras(G12D) cooperate to promote murine pancreatic tumorigenesis recapitulating human intraductal papillary mucinous neoplasm. *Oncogene* **35**: 2407-2412.

Tammela T, Sanchez-Rivera FJ, Cetinbas NM, Wu K, Joshi NS, Helenius K, Park Y, Azimi R, Kerper NR, Wesselhoeft RA. 2017. A Wnt-producing niche drives proliferative potential and progression in lung adenocarcinoma. *Nature* **545**: 355.

Taylor SS, Kim C, Cheng CY, Brown SH, Wu J, Kannan N. 2008. Signaling through cAMP and cAMP-dependent protein kinase: diverse strategies for drug design. *Biochim Biophys Acta* **1784**: 16-26.

Ting H-A, von Moltke J. 2019. The immune function of tuft cells at gut mucosal surfaces and beyond. *The Journal of Immunology* **202**: 1321-1329.

Travis WD, Brambilla E, Noguchi M, Nicholson AG, Geisinger K, Yatabe Y, Powell CA, Beer D, Riely G, Garg K et al. 2011. International Association for the Study of Lung Cancer/American Thoracic Society/European Respiratory Society: international multidisciplinary classification of lung adenocarcinoma: executive summary. *Proceedings of the American Thoracic Society* **8**: 381-385.

Trejo CL, Juan J, Vicent S, Sweet-Cordero A, McMahon M. 2012. MEK1/2 inhibition elicits regression of autochthonous lung tumors induced by KRASG12D or BRAFV600E. *Cancer research* **72**: 3048-3059.

Tsai J, Lee JT, Wang W, Zhang J, Cho H, Mamo S, Bremer R, Gillette S, Kong J, Haass NK. 2008. Discovery of a selective inhibitor of oncogenic B-Raf kinase with potent antimelanoma activity. *Proceedings of the National Academy of Sciences* **105**: 3041-3046.

Tuveson DA, Shaw AT, Willis NA, Silver DP, Jackson EL, Chang S, Mercer KL, Grochow R, Hock H, Crowley D. 2004. Endogenous oncogenic K-rasG12D stimulates proliferation and widespread neoplastic and developmental defects. *Cancer cell* **5**: 375-387.

Vallone VF, Leprovots M, Strollo S, Vasile G, Lefort A, Libert F, Vassart G, Garcia M-I. 2016. Trop2 marks transient gastric fetal epithelium and adult regenerating cells after epithelial damage. *Development* **143**: 1452-1463.

VanDussen KL, Marinshaw JM, Shaikh N, Miyoshi H, Moon C, Tarr PI, Ciorba MA, Stappenbeck TS. 2015. Development of an enhanced human gastrointestinal epithelial culture system to facilitate patient-based assays. *Gut* **64**: 911-920.

Winslow MM, Dayton TL, Verhaak RG, Kim-Kiselak C, Snyder EL, Feldser DM, Hubbard DD, DuPage MJ, Whittaker CA, Hoersch S. 2011. Suppression of lung adenocarcinoma progression by Nkx2-1. *Nature* **473**: 101.

Xu C, Su Z. 2015. Identification of cell types from single-cell transcriptomes using a novel clustering method. *Bioinformatics* **31**: 1974-1980.

Young NP, Crowley D, Jacks T. 2011. Uncoupling cancer mutations reveals critical timing of p53 loss in sarcomagenesis. *Cancer research* **71**: 4040-4047.

Zhan T, Ambrosi G, Wandmacher AM, Rauscher B, Betge J, Rindtorff N, Häussler RS, Hinsenkamp I, Bamberg L, Hessling B. 2019. MEK inhibitors activate Wnt signalling and induce stem cell plasticity in colorectal cancer. *Nature communications* **10**: 1-17.

Zhan T, Rindtorff N, Boutros M. 2017. Wnt signaling in cancer. *Oncogene* **36**: 1461-1473.

Zhang P, Yang M, Zhang Y, Xiao S, Lai X, Tan A, Du S, Li S. 2019. Dissecting the Single-Cell Transcriptome Network Underlying Gastric Premalignant Lesions and Early Gastric Cancer. *Cell reports* **27**: 1934-1947. e1935.

Zhang Y, Wang R, Li Y, Pan Y, Hu H, Zhang Y, Li H, Shen L, Yu Y, Sun Y et al. 2015. Negative Thyroid Transcription Factor 1 Expression Defines an Unfavorable Subgroup of Lung Adenocarcinomas. *Journal of Thoracic Oncology* **10**: 1444-1450.

FIG 1

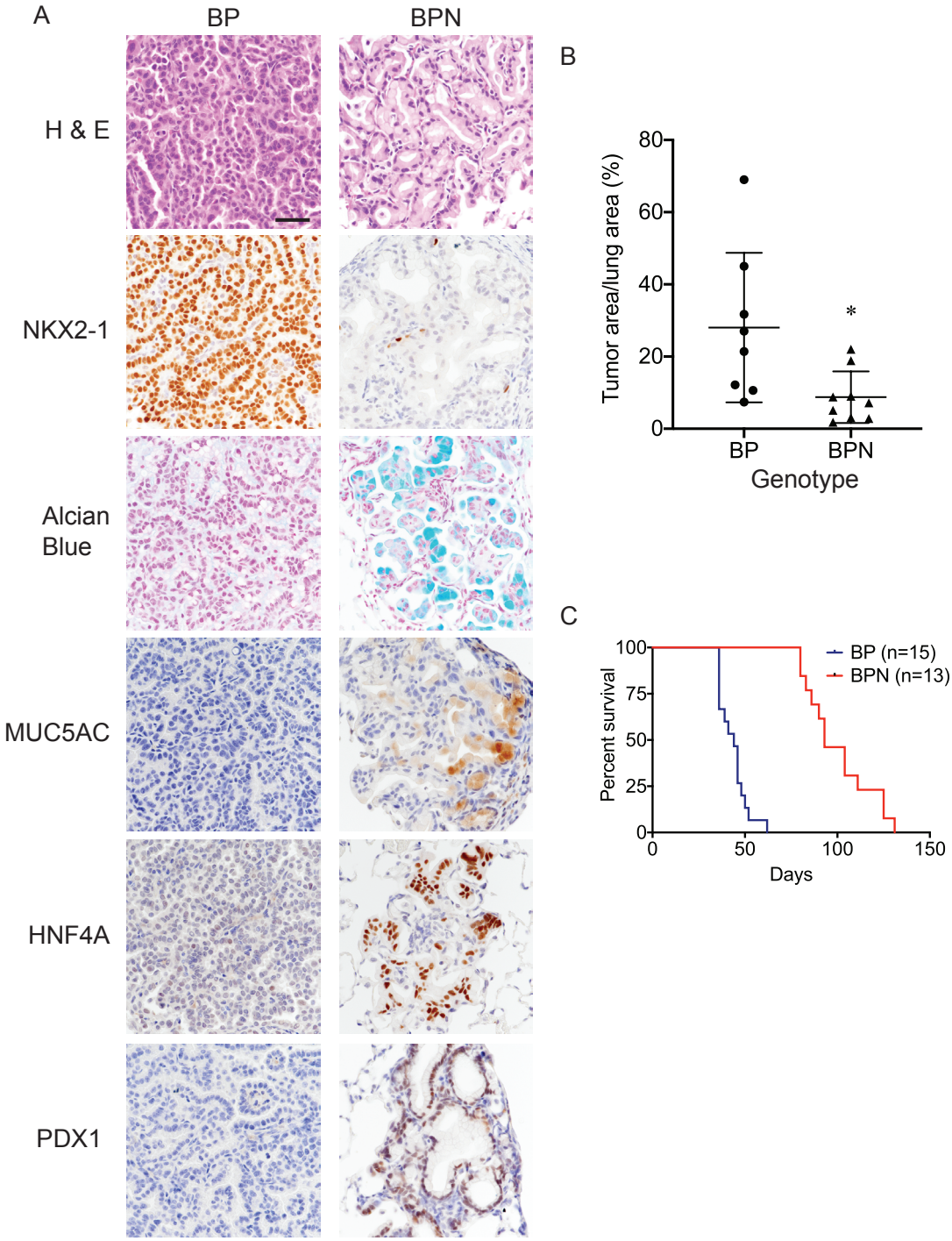
A
BP
BPN
H & E
NKX2-1
Alcian Blue
MUC5AC
HNF4A
PDX1
B
Tumor area/lung area (%)
80
60
40
20
0
*
BP
BPN
Genotype
C
Percent survival
100
75
50
25
0
0
50
100
150
Days
BP (n=15)
BPN (n=13)

Figure 1. *Nkx2-1* deletion induces mucinous adenocarcinoma but impairs tumor initiation in BRAF^{V600E}-driven lung adenocarcinoma. (A) Representative photomicrographs of lung neoplasia arising 8 weeks after initiation with PGK-Cre lentivirus (5x10^3 pfu/mouse). BP mice are *BRaf$^{CA/+}$;Trp53$^{f/f}$;Nkx2-1$^{f/+}$;Rosa26$^{tdTomato/tdTomato}$*. BPN mice are *BRaf$^{CA/+}$;Trp53$^{f/f}$;Nkx2-1$^{f/f}$;Rosa26$^{tdTomato/tdTomato}$*. Hematoxylin and eosin (H&E), Alcian blue stain for mucin production, and immunohistochemistry (IHC) for NKX2-1, plus, markers of gastrointestinal differentiation. Scale bar: 100 μm. (B) Quantitation of lung tumor burden 8 weeks after initiation with PGK-Cre lentivirus (5x10^3 pfu/mouse) in indicated genotypes of mice: BP (n=8), BPN (n=9). *P = 0.019 by Student's *t*-test. (C) Long-term survival after tumor initiation with Ad5-CMV-Cre adenovirus (2.5x10^7 pfu/mouse) in mice of indicated genotypes. P < 0.0001 by Log-rank test.

FIG 2

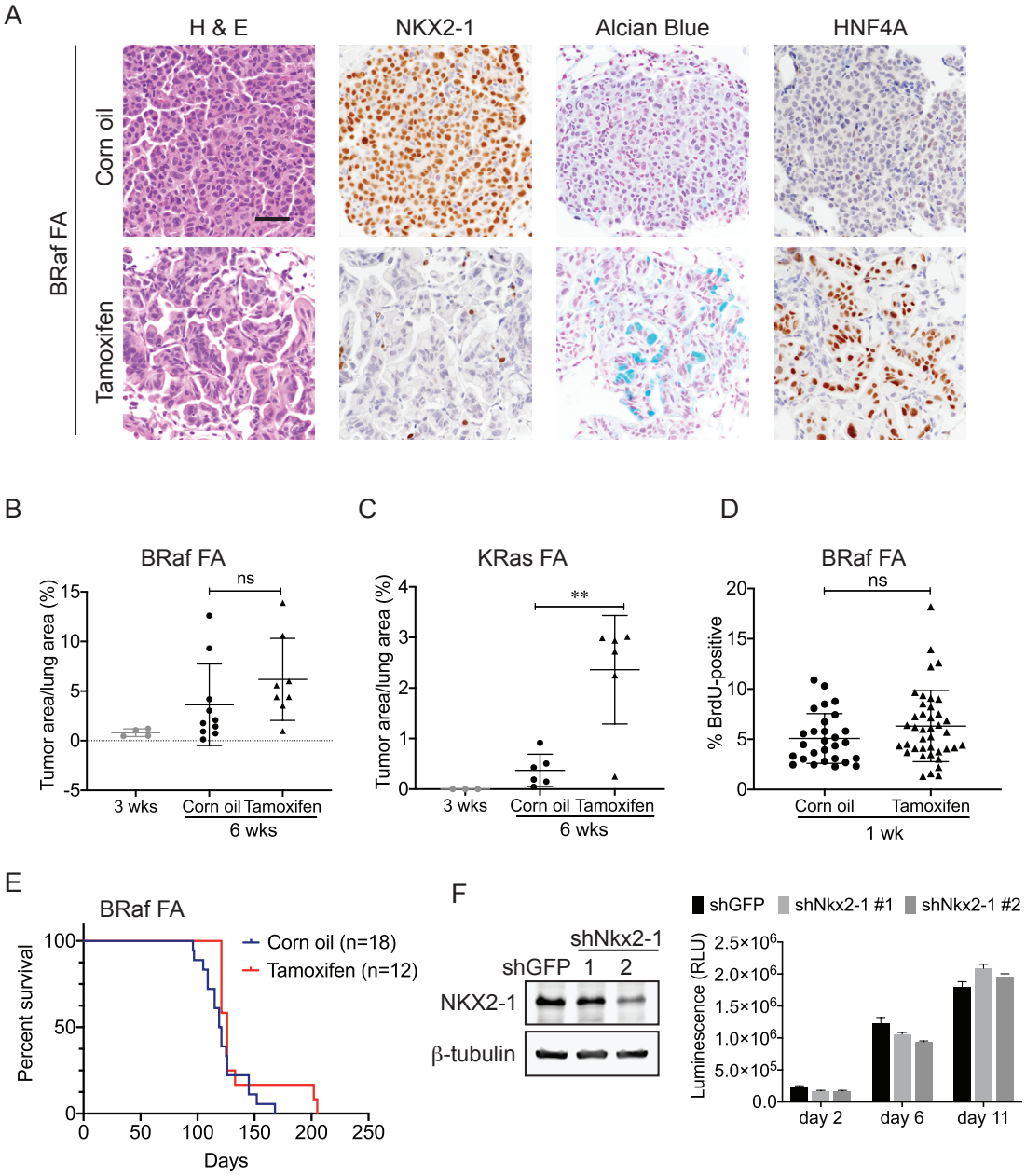
A
H & E
NKX2-1
Alcian Blue
HNF4A
BRaf FA
Corn oil
Tamoxifen
B
BRaf FA
ns
Tumor area/lung area (%)
3 wks
Corn oil
Tamoxifen
6 wks
C
KRas FA
**
Tumor area/lung area (%)
3 wks
Corn oil
Tamoxifen
6 wks
D
BRaf FA
ns
% BrdU-positive
Corn oil
Tamoxifen
1 wk
E
BRaf FA
Corn oil (n=18)
Tamoxifen (n=12)
Percent survival
Days
F
shNkx2-1
shGFP
1
2
NKX2-1
β-tubulin
shGFP
shNkx2-1 #1
shNkx2-1 #2
Luminescence (RLU)
day 2
day 6
day 11

Figure 2. *Nkx2-1* deletion does not augment growth of established BRAF-mutant LUAD.

(A, B) All mice are *BRaf*$^{FA/+}$;*Trp53*$^{frt/frt}$;*Nkx2-1*$^{f/f}$;*Rosa26*$^{CreERT2/CreERT2}$. Viral FlpO-recombinase expression simultaneously activated BRAF^{V600E} and Cre^{ERT2} and deleted *Trp53* by excision of *Frt* sites. 3 weeks post-tumor initiation, mice were injected with corn oil (as vehicle control) or with tamoxifen to recombine *LoxP*-sites within *Nkx2-1* alleles by Cre^{ERT2} recombinase. Lungs were harvested 3 weeks thereafter. (A) H&E, Alcian blue, NKX2-1 and HNF4A staining of lung neoplasia arising 6 weeks after initiation with Ad-FlpO adenovirus (2x10^{7} pfu/mouse). Scale bar: 100 μm. (B) Quantification of tumor burden at 3 weeks (n=4 mice), and at 6 weeks after initiation, following corn oil treatment (n=10 mice) or tamoxifen injections (n=8 mice). Tamoxifen administration consisted of 6 intraperitoneal doses over 9 days. Graphs represent mean ± S.D. *P* values are not statistically significant. (C) Mice are *KRas*$^{frtSfrt\text{-}G12D/+}$;*Trp53*$^{frt/frt}$;*Nkx2-1*$^{f/f}$;*Rosa26*$^{CreERT2/CreERT2}$ and were administered with corn oil (n=6 mice) or tamoxifen (n=6 mice) injections as described in (B). Shown is the quantification of tumor burden at 3 weeks and at 6 weeks post-initiation. Graphs represent mean ± S.D. ***P*=0.0014 by Student's *t*-test. (D) Quantitation of BrdU incorporation 1 week after deletion of *Nkx2-1*. Lung neoplasia was initiated with Ad-FlpO adenovirus (2x10^{7} pfu/mouse) in *BRaf*$^{FA/+}$;*Trp53*$^{frt/frt}$;*Nkx2-1*$^{f/f}$;*Rosa26*$^{CreERT2/CreERT2}$ mice. At 6 weeks post-initiation, mice were administered with 4 daily doses of vehicle or tamoxifen injections and analyzed at 7 weeks. Graphs represent mean ± S.D. Corn oil (28 tumors from 3 mice), tamoxifen (40 tumors from 4 mice) were analyzed. (E) Survival of *BRaf*$^{FA/+}$;*Trp53*$^{frt/frt}$;*Nkx2-1*$^{f/f}$;*Rosa26*$^{CreERT2/CreERT2}$ mice that were treated with tamoxifen or vehicle starting at 3

weeks following tumor initiation. Tamoxifen administration consisted of 6 intraperitoneal doses over 9 days, followed by tamoxifen-containing chow for 1 month. (F) Immunoblot for NKX2-1 protein levels in a human $BRAF^{V600E}$-positive LUAD cell line, HCC364, that is stably expressing short hairpins against *GFP* or *Nkx2-1*. β-tubulin serves as loading control. Cell proliferation of control HCC364 cells versus HCC364 cells harboring knockdown of *Nkx2-1* was measured by CellTiter-Glo Luminescent cell viability assay at the indicated timepoints. Graph represents mean ± S.D. Experiment was done twice.

FIG 3

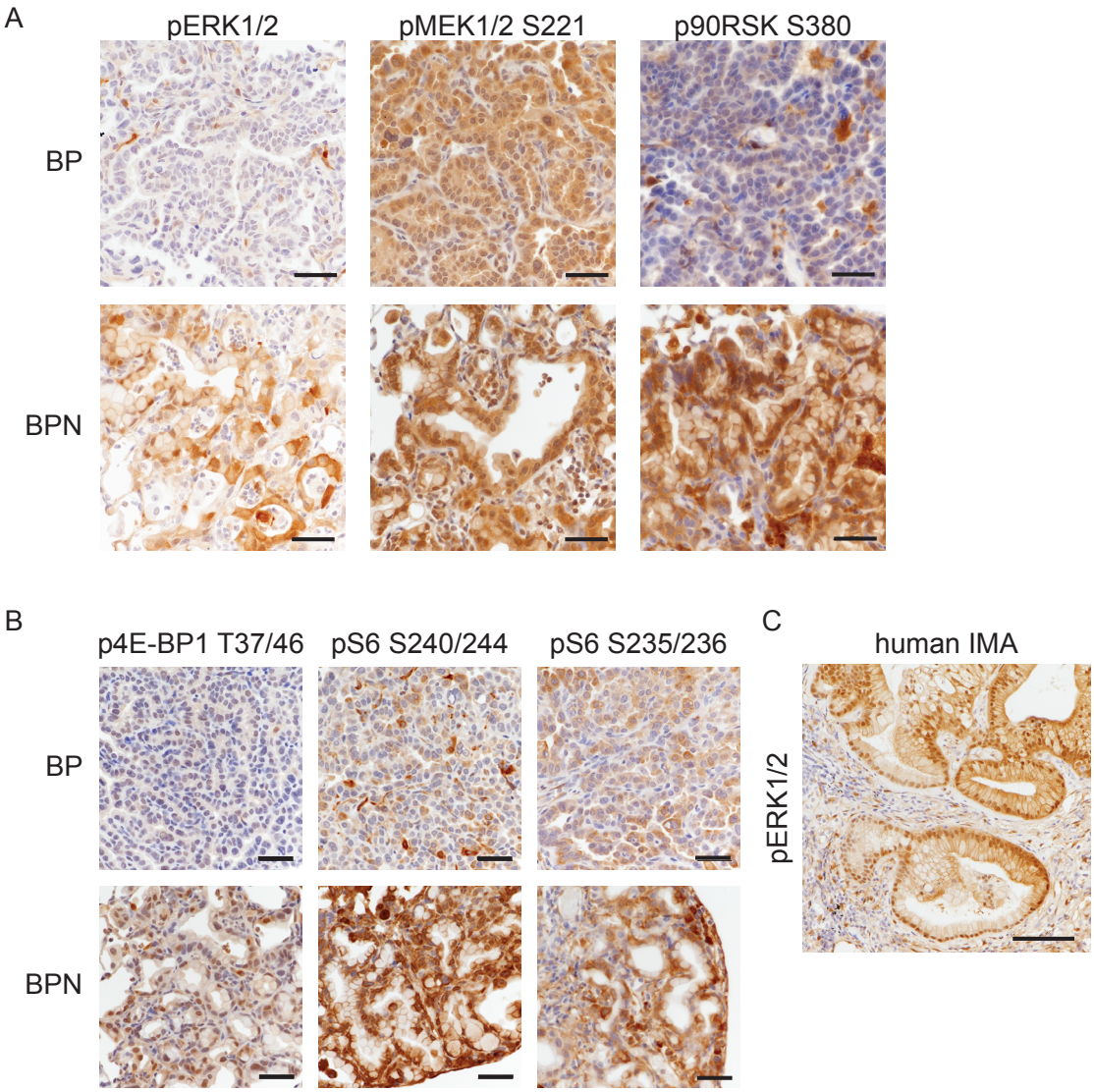
A
pERK1/2
pMEK1/2 S221
p90RSK S380
BP
BPN
B
p4E-BP1 T37/46
pS6 S240/244
pS6 S235/236
BP
BPN
C
human IMA
pERK1/2

Figure 3. NKX2-1 regulates MAPK pathway in BRAF^{V600E}-driven LUAD.

(A, B) IHC for indicated proteins in lung neoplasia present at 8 weeks post-initiation in *BRaf$^{CA/+}$;Trp53$^{f/f}$;Nkx2-1$^{f/+}$;Rosa26$^{tdTomato/tdTomato}$* and *BRaf$^{CA/+}$;Trp53$^{f/f}$;Nkx2-1$^{f/f}$;Rosa26$^{tdTomato/tdTomato}$* mice. (C) A representative staining of phospho-ERK in a human IMA. Scale bar: 100 μm.

FIG 4

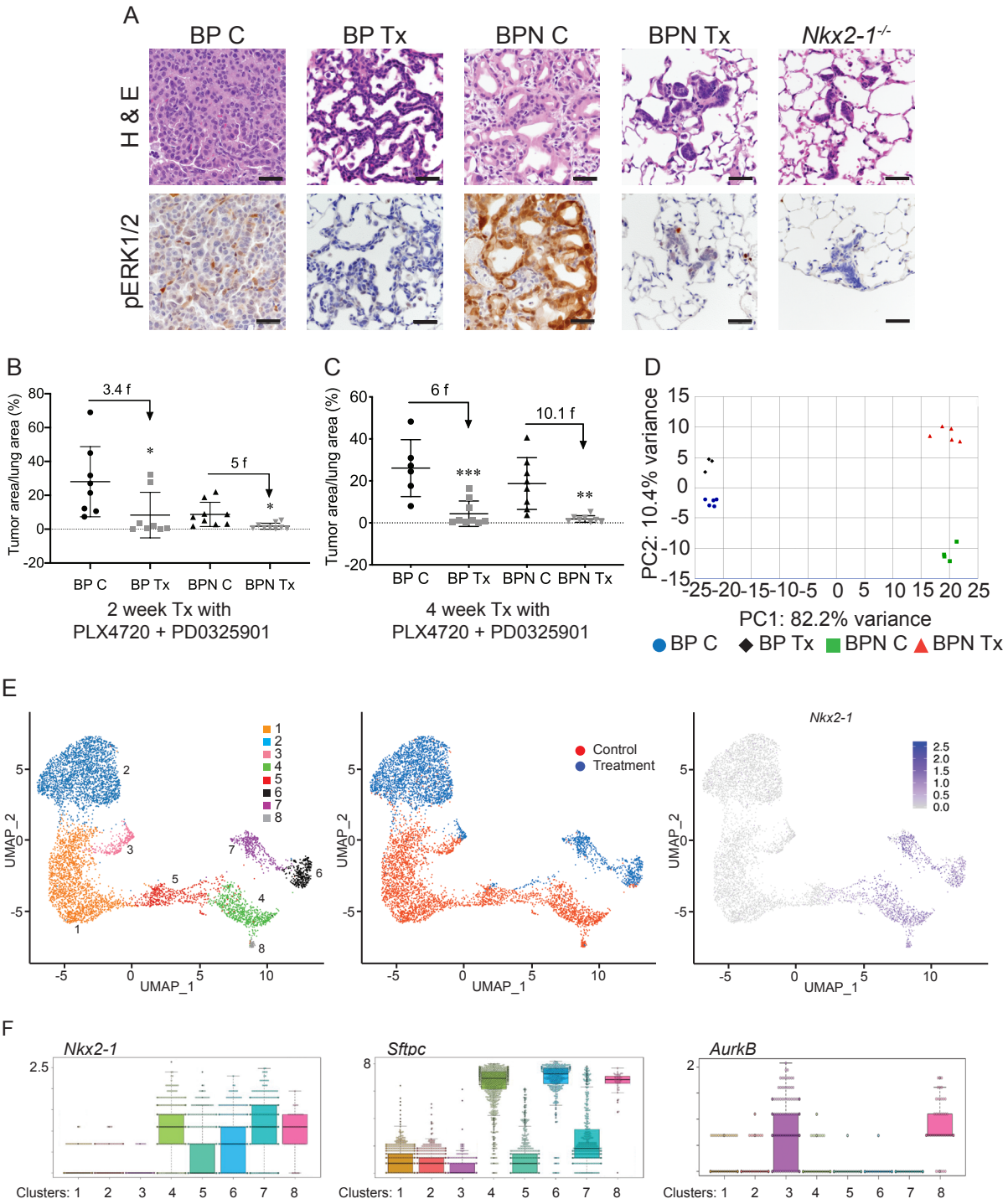
A
BP C
BP Tx
BPN C
BPN Tx
Nkx2-1-/-
H & E
pERK1/2
B
Tumor area/lung area (%)
3.4 f
5 f
BP C
BP Tx
BPN C
BPN Tx
2 week Tx with
PLX4720 + PD0325901
C
Tumor area/lung area (%)
6 f
10.1 f
4 week Tx with
PLX4720 + PD0325901
D
PC2: 10.4% variance
PC1: 82.2% variance
BP C
BP Tx
BPN C
BPN Tx
E
UMAP_1
UMAP_2
Control
Treatment
Nkx2-1
F
Nkx2-1
Sftpc
AurkB
Clusters: 1 2 3 4 5 6 7 8

Figure 4. NKX2-1 status modulates response to MAPK pathway inhibitors

(A) Representative H&E and phospho-ERK1/2 immunostaining photomicrographs of paraffin-embedded lung sections from *BRaf*$^{CA/+}$*;Trp53*$^{f/f}$*;Nkx2-1*$^{f/+}$*;Rosa26*$^{tdTomato/tdTomato}$ and *BRaf*$^{CA/+}$*;Trp53*$^{f/f}$*;Nkx2-1*$^{f/f}$*;Rosa26*$^{tdTomato/tdTomato}$ mice that were treated with control chow (BP C/BPN C) or chow containing PLX4720 (200 mg/kg) and PD0325901 (7 mg/kg) inhibitors (BP Tx/BPN Tx) for two weeks starting at 6 weeks post-tumor initiation with PGK-Cre lentivirus (5x10^3 pfu/mouse). Scale bar: 100 µm. (B, C) Quantification of tumor burden in BP and BPN mice that were fed control chow or chow containing MAPK inhibitors starting at 6 weeks post-tumor initiation with PGK-Cre lentivirus (5x10^3 pfu/mouse). Graphs represent mean ± S.D. (B) Chow treatment lasted 2 weeks and lungs were harvested at the 8 week timepoint. BP C (n=8), BP Tx (n=8), BPN C (n=9), BPN Tx (n=9). *P<0.05 by Student's t-test. Numbers indicated above graphs represent the fold reduction in tumor burden upon inhibitor-chow administration. (C) Chow treatment lasted 4 weeks and lungs were harvested at the 10 week timepoint. BP C (n=6), BP Tx (n=9), BPN C (n=8), BPN Tx (n=8). **P < 0.01, ***P<0.001. Numbers indicated above graphs represent the fold reduction in tumor burden with inhibitor-chow administration. (D) Global gene expression analyses were performed on RNAs from FACS-sorted tdTomato$^+$ BP C (n=5), BP Tx (n=3), BPN C (n=4) and BPN Tx (n=5) murine lung tumor cells isolated at 7 weeks following initiation with Ad5-Spc-Cre adenovirus (5x10^8 pfu/mouse for BP and 8x10^8 pfu/mouse for BPN mice). Control and MAPK-inhibitor chow treatments were given for 1 week at 6 weeks post-adenoviral instillation. Shown is the principal-component analysis (PCA) plot of the top 500 most variable genes showing that the four experimental groups of lung tumors, BP C, BP Tx, BPN C and BPN Tx, had distinct global patterns of

gene expression. (E) UMAP plots showing relatedness of high quality, tumor cell scRNA-seq profiles from BPN control (n=2) and BPN MAPKi-treated (n=2) mice. Tumor cluster designations are indicated (left). Control and treated cells indicated (middle). *Nkx2-1* expression in scRNA-seq data indicating that clusters 4-8 represent incomplete recombinants (right). Single tumor cells were obtained by FACS-sorting tdTomato^{+} cells isolated at 7 weeks following initiation with Ad5-Spc-Cre adenovirus ($8x10^{8}$ pfu/mouse). Control and MAPK-inhibitor chow treatments were given for 1 week at 6 weeks post-adenoviral instillation. (F) Beeswarm plots of single cell sequencing data showing expression levels of *Nkx2-1*, *Sftpc* and *AurkB* transcripts in tumor clusters 1-8.

FIG 5

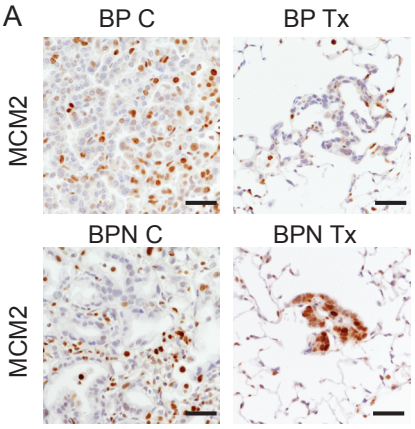

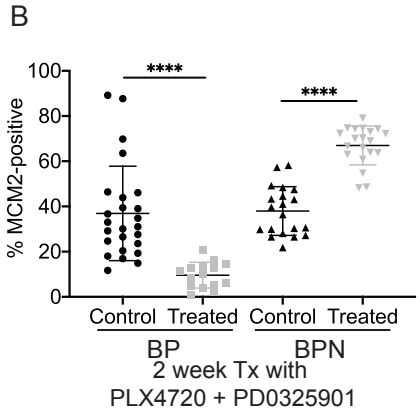

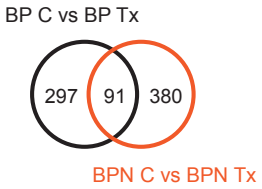

D

BP C vs BP Tx: Gene Ontology analysis by Illumina Correlation Engine				
BIOGROUP NAME	SCORE	COMMON GENES	DIRECTION	P-VALUE
cell division	105.76	41	up	1.20E-46
mitosis	104.37	36	up	4.70E-46
nuclear division	104.37	36	up	4.70E-46
kinetochore	51.24	16	up	5.60E-23
spindle	49.21	17	up	4.30E-22

E

BPN C vs BPN Tx: Gene Ontology analysis by Illumina Correlation Engine				
BIOGROUP NAME	SCORE	COMMON GENES	DIRECTION	P-VALUE
extracellular matrix	46.96	24	up	4.00E-21
proteinaceous extracellular matrix	46.76	23	up	4.90E-21
vascular development	23.87	16	up	4.30E-11
tissue morphogenesis	23.28	16	up	7.70E-11
regulation of vascular development	19.58	10	up	3.10E-09

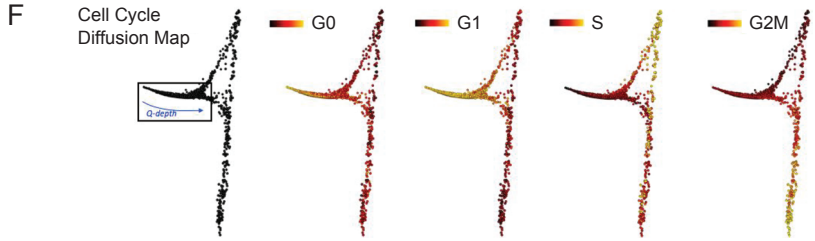

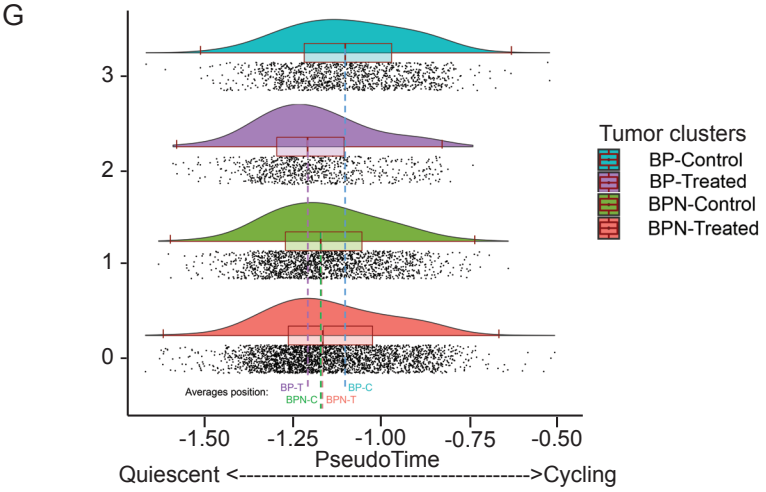

Figure 5. Differential impact of MAPK inhibitors on the cell cycle in NKX2-1-positive and NKX2-1-negative tumors

(A, B) Immunostaining for and quantitation of the proliferation marker MCM2 in tumors from BP and BPN mice at 8 weeks post-initiation. Control or MAPK-inhibitor infused chow feeding started at 6 weeks and was maintained for 2 weeks. BP C (25 tumors from 4 mice), BP Tx (15 tumors from 3 mice), BPN C (20 tumors from 3 mice), BPN Tx (20 tumors from 3 mice). Scale bar: 100 μm. Graphs represent mean ± S.D. ****P<0.0001 by Student's t-test. (C) Venn diagram of the number of genes that were commonly and uniquely altered in BP versus BPN tumors upon combined mBRAFi + MEKi chow treatment. P_{adj} < 0.1. (D, E) Lists of the top-scoring Gene Ontology pathway terms of differentially expressed genes between control- and drug-chow treated BP (D) or BPN (E) tumors, as determined by Illumina Correlation Engine analyses of bulk RNAseq data. UP = enriched in control relative to treated samples. (F) Diffusion map of cell cycle phase signatures in scRNA-seq data showing coherent enrichment for phase specific signatures at specific graphical regions. >80% of cells are disturbed in the box that correlates with G0 and G1 signatures and along which we fit a principle curve to model likely depth of quiescence (Q-depth). (G) Positioning of scRNA-seq profiles from the indicated cell clusters along the Q-depth curve. BPN control = cluster 1; BPN treated = cluster 2; BP control = cluster 4+5; BP treated = cluster 6+7.

FIG 6

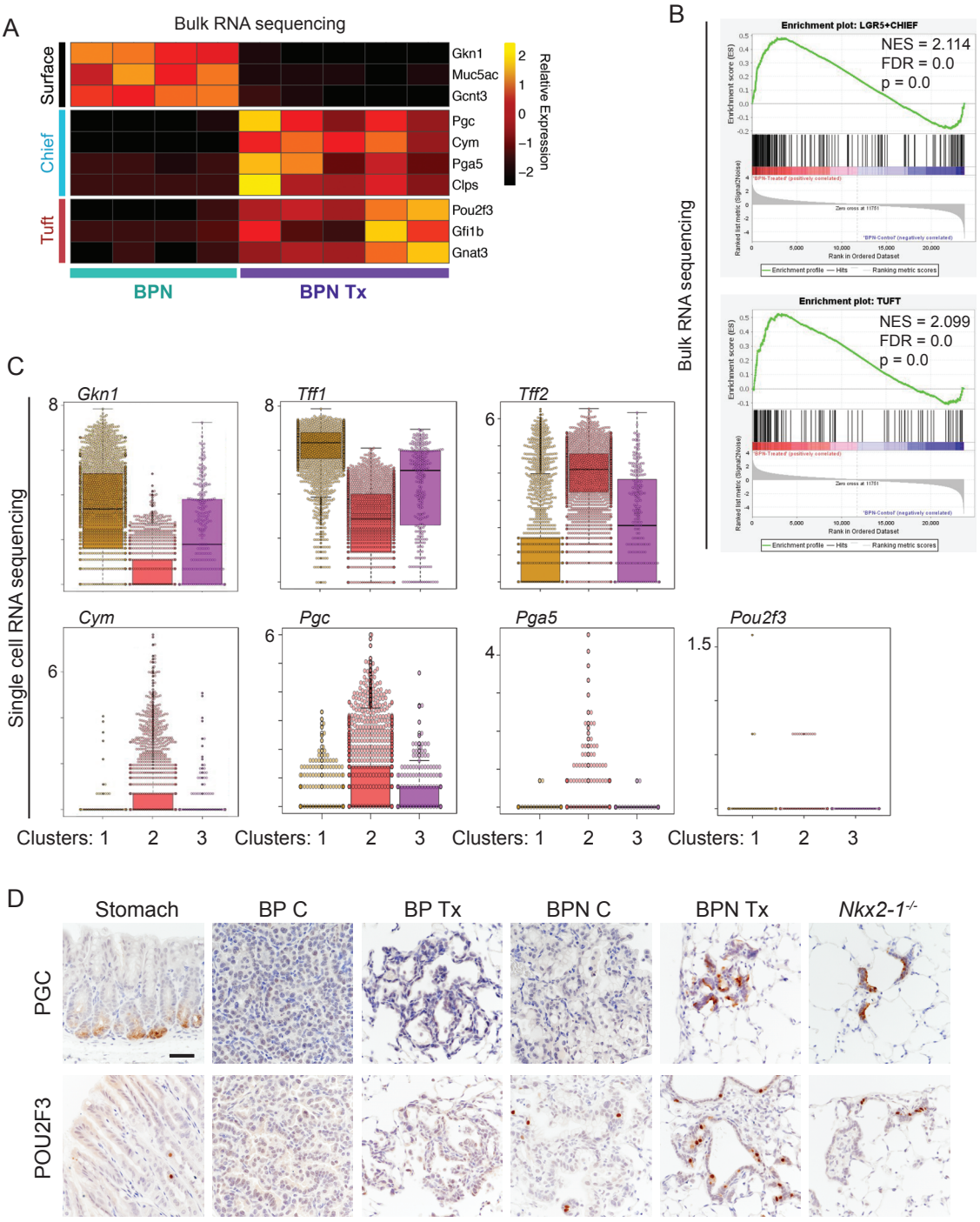
A
Bulk RNA sequencing
Surface
Chief
Tuft
Gkn1
Muc5ac
Gcnt3
Pgc
Cym
Pga5
Clps
Pou2f3
Gfi1b
Gnat3
Relative Expression
BPN
BPN Tx
B
Bulk RNA sequencing
Enrichment plot: LGR5+CHIEF
NES = 2.114
FDR = 0.0
p = 0.0
Enrichment plot: TUFT
NES = 2.099
FDR = 0.0
p = 0.0
C
Single cell RNA sequencing
Gkn1
Tff1
Tff2
Cym
Pgc
Pga5
Pou2f3
Clusters: 1 2 3
D
Stomach
BP C
BP Tx
BPN C
BPN Tx
Nkx2-1-/-
PGC
POU2F3

Figure 6. MAPK activity regulates cellular identity in NKX2-1-negative tumors

(A) Transcriptome analysis comparing control BPN cells with drug-treated BPN tumor cells. Heatmap depicts gastric surface mucous cell markers whose expression diminished versus gastric chief cell or tuft cell markers whose expression increased in MAPK-inhibitor treated BPN cells relative to untreated. *adjP*<0.05 for each comparison. RNAseq data was derived from tdTomato-expressing tumor cells FACS-sorted from BPN mice. 6 weeks after tumor initiation, mice were treated for 1 week with control chow (n=4) or chow containing $BRAF^{V600E}$ inhibitor plus MEK inhibitor (n=5). (B) GSEA against chief and tuft cell signatures. (C) Beeswarm plots of single cell sequencing data showing expression levels of *Gkn1*, *Tff1*, *Tff2*, *Cym*, *Pgc*, *Pga5* and *Pou2f3* transcripts in BPN tumor clusters 1-3 and highlighting key drug-mediated cell-identity changes. (D) IHC for a gastric chief cell marker (Pepsinogen C) and a tuft cell marker (POU2F3) on LUAD sections derived 7 weeks following tumor initiation with PGK-Cre lentivirus ($5x10^3$ pfu/mouse). At 6 weeks, $BRaf^{CA/+};Trp53^{f/f};Nkx2\text{-}1^{f/+};Rosa26^{tdTomato/tdTomato}$ and $BRaf^{CA/+};Trp53^{f/f};Nkx2\text{-}1^{f/f};Rosa26^{tdTomato/tdTomato}$ mice were given control or MAPK-inhibitor chow for 1 week. Also shown are sections of normal stomach epithelium as positive controls for immunostaining. Note that in hyperplasia that arise from *Nkx2-1* deletion in distal lung without concomitant oncogenic activation also upregulate these lineage-restricted markers. $Nkx2\text{-}1^{f/f}$ mice were infected with Ad5-Spc-Cre (10^9 pfu/mouse). Lungs were harvested 16 weeks later. Scale bar: 100 μm.

FIG 7

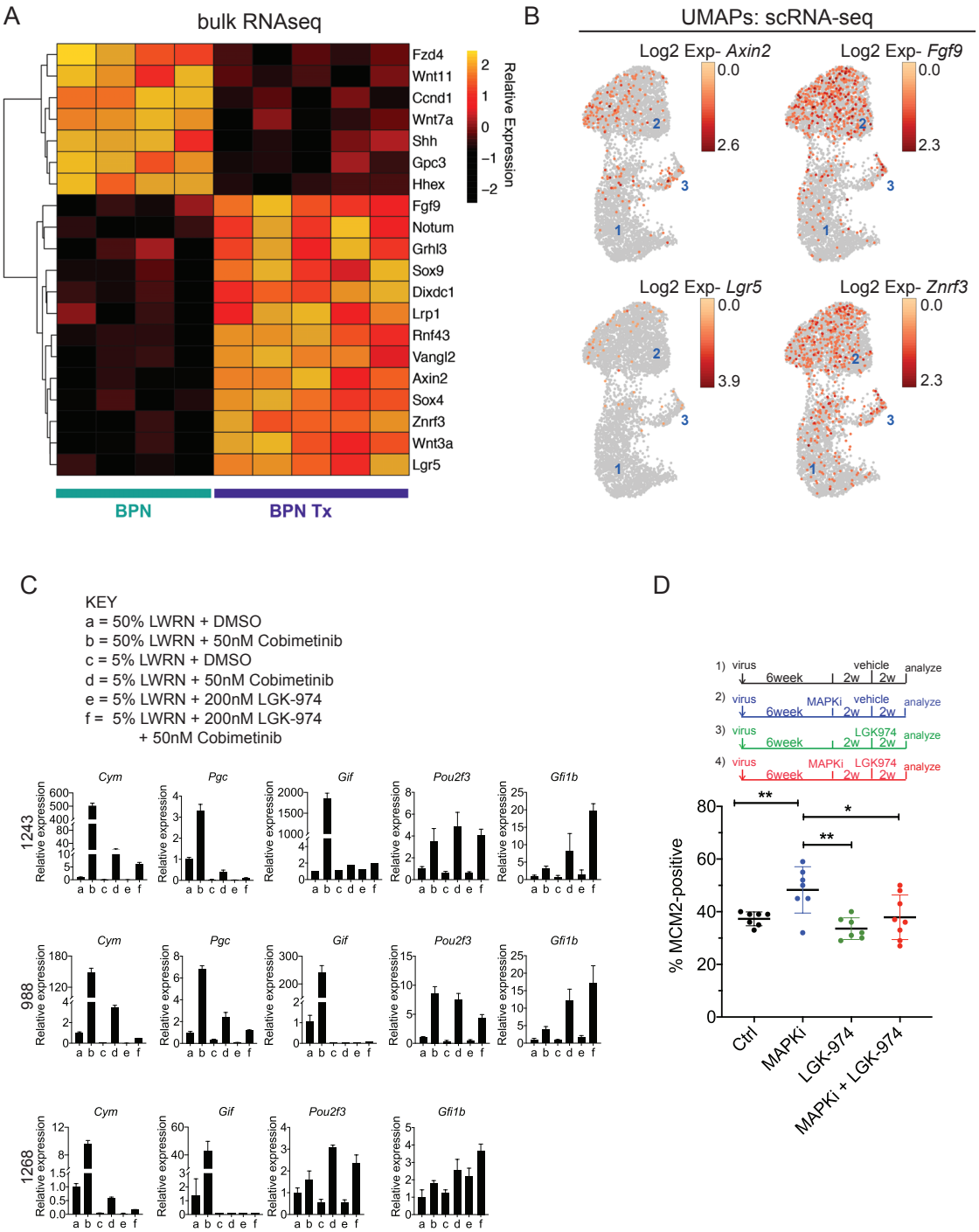
A
bulk RNAseq
Fzd4
Wnt11
Ccnd1
Wnt7a
Shh
Gpc3
Hhex
Fgf9
Notum
Grhl3
Sox9
Dixdc1
Lrp1
Rnf43
Vangl2
Axin2
Sox4
Znrf3
Wnt3a
Lgr5
Relative Expression
BPN
BPN Tx
B
UMAPs: scRNA-seq
Log2 Exp- Axin2
Log2 Exp- Fgf9
Log2 Exp- Lgr5
Log2 Exp- Znrf3
C
KEY
a = 50% LWRN + DMSO
b = 50% LWRN + 50nM Cobimetinib
c = 5% LWRN + DMSO
d = 5% LWRN + 50nM Cobimetinib
e = 5% LWRN + 200nM LGK-974
f = 5% LWRN + 200nM LGK-974
+ 50nM Cobimetinib
1243
988
1268
Cym
Pgc
Gif
Pou2f3
Gfi1b
Relative expression
D
virus
vehicle
MAPKi
LGK974
analyze
6week
2w
% MCM2-positive
Ctrl
MAPKi
LGK-974
MAPKi + LGK-974

Figure 7. MAPK inhibition activates WNT signaling, which mediates lineage switching. (A) Transcriptome analysis of genes comprising the canonical WNT pathway gene ontology (AmiGO) in RNA purified from FACS-sorted BPN tumor cells 1 week post-treatment with PLX4720+PD0325901 or control chow. *adjP*<0.05 for each comparison. Color key indicates normalized expression levels (Log10). (B) UMAP plots of single cell sequencing data in tumor clusters 1-3 showing expression levels of *Axin2*, *Lgr5, Fgf9* and *Znrf3* transcripts, which are readouts of canonical WNT signaling. (C) WNT pathway inhibition partially blocks shift in cellular identity. Analyses of indicated gene expression levels in BPN (1243 and 988) and KPN (1268) tumor organoid lines by qRT-PCR at 24 hours and under different treatment conditions. Organoids were cultured in 50% L-WRN (a, b) or reduced 5% L-WRN media (c, d, e, f) and treated with DMSO (a, c), single agent Cobimetinib (b, d) or the Porcupine inhibitor, LGK-974 (e), and both inhibitors (f). Graphs indicate mean±S.D. Experiment was reproducibly performed 2-3 times. (D) Quantitation of the proliferation marker MCM2 in 10 week autochthonous BPN lung tumors under four different treatment conditions: 1) control (n=7); 2) MAPK-inhibitor chow (n=7); 3) LGK-974 (n=7); and 4) MAPK-inhibitor chow and LGK-974 (n=8).

Suppl FIG S1

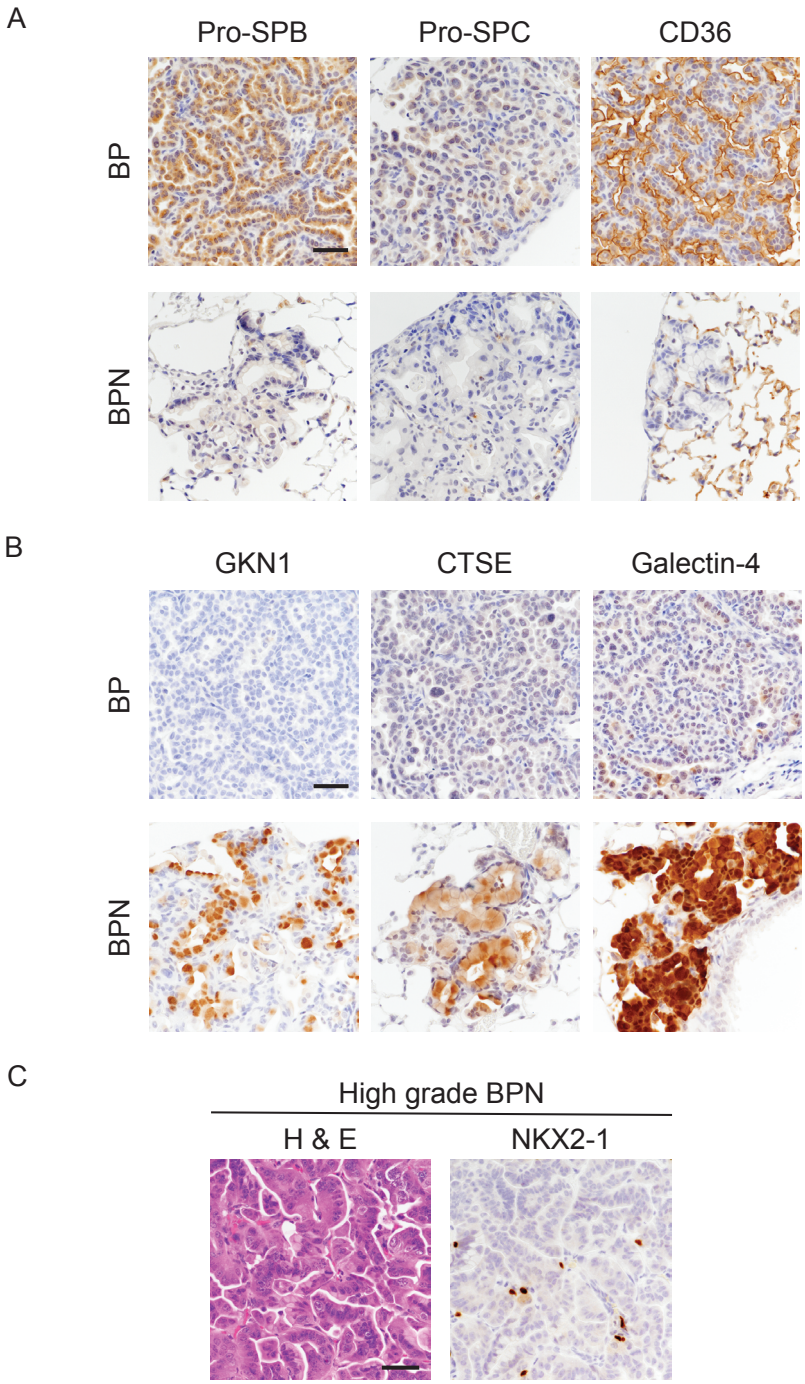
A
Pro-SPB
Pro-SPC
CD36
BP
BPN
B
GKN1
CTSE
Galectin-4
BP
BPN
C
High grade BPN
H & E
NKX2-1

Figure S1. *Nkx2-1* deletion concomitant with activation of BRAF^{V600E} induces mucinous adenocarcinoma formation. (A, B) Histologic phenotype of lung neoplasia arising 8 weeks after initiation with PGK-Cre lentivirus ($5x10^3$ pfu/mouse) in *BRaf$^{CA/+}$;Trp53 $^{f/f}$;Nkx2-1$^{f/+}$;Rosa26$^{tdTomato/tdTomato}$* (BP) and *BRaf$^{CA/+}$;Trp53$^{f/f}$;Nkx2-1$^{f/f}$;Rosa26$^{tdTomato/tdTomato}$* (BPN) mice. Immunostaining for markers of pulmonary (A) and gastrointestinal (B) differentiation. (C) H&E and NKX2-1 IHC of a representative high grade BPN lung tumor. Scale bar: 100 μm.

Suppl FIG 2

A

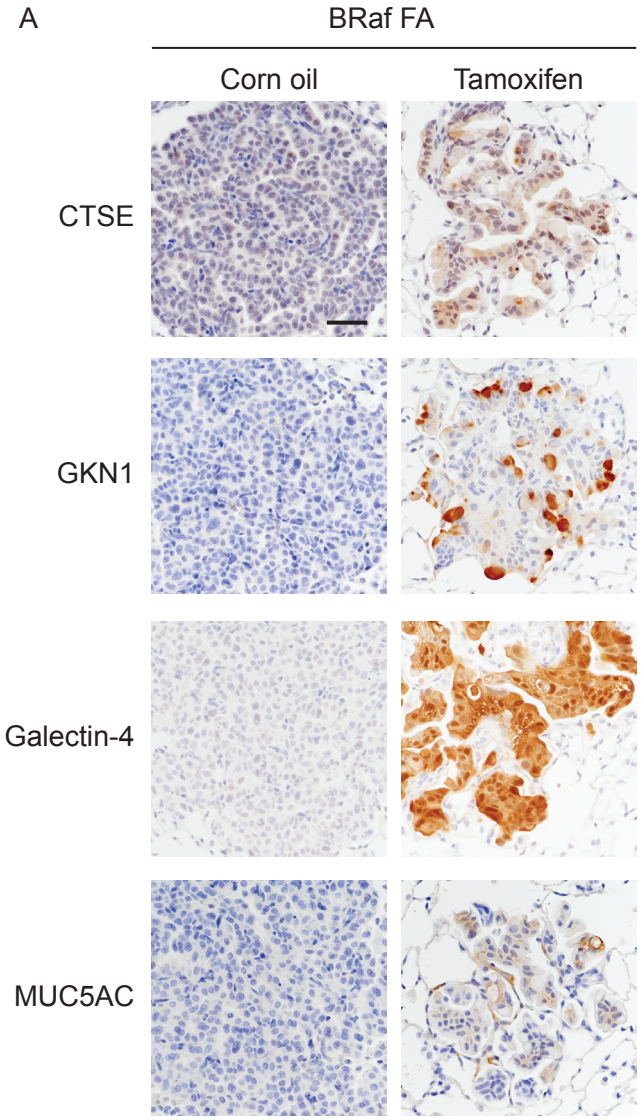

B

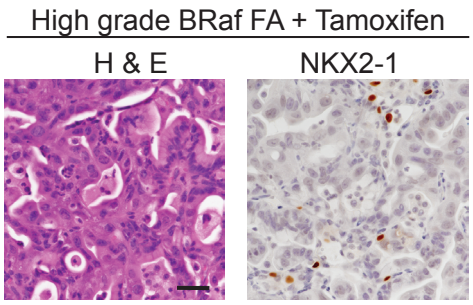

Figure S2. *Nkx2-1* loss in established BRAF^{V600E}-driven tumors promotes gastric differentiation. (A) Immunostaining for indicated mucin/gastric markers in NKX2-1-positive and -negative LUADs. Lung tumor sections were obtained from corn oil or tamoxifen treated *BRaf$^{FA/+}$;Trp53$^{frt/frt}$;Nkx2-1$^{f/f}$;Rosa26$^{CreERT2/CreERT2}$* mice 6 weeks post-initiation with Ad-FlpO adenovirus ($2x10^7$ pfu/mouse). Scale bar: 100 μm. (B) Representative images of high grade tumors obtained from a BRaf FA mouse that had received Tamoxifen injections. Scale bar: 100 μm.

Suppl FIG 3

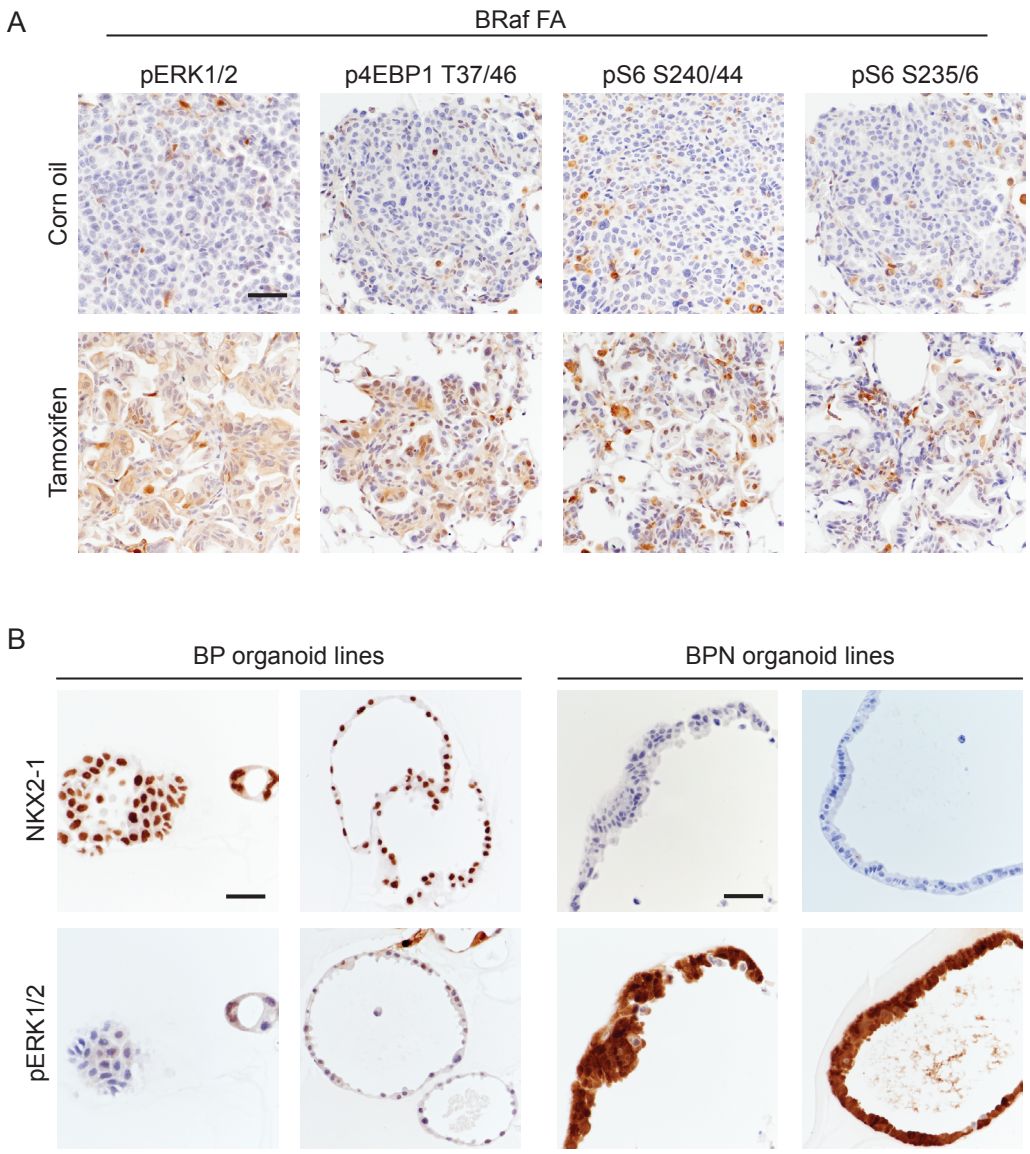
A
BRaf FA
pERK1/2
p4EBP1 T37/46
pS6 S240/44
pS6 S235/6
Corn oil
Tamoxifen
B
BP organoid lines
BPN organoid lines
NKX2-1
pERK1/2

Figure S3: NKX2-1 regulates MAPK pathway in BRAF^{V600E}-driven LUAD.

(A) IHC for indicated phospho-proteins in NKX2-1-positive and -negative LUADs. Lung tumor sections were obtained from corn oil or tamoxifen treated *BRaf$^{FA/+}$;Trp53$^{frt/frt}$;Nkx2-1$^{f/f}$;Rosa26$^{CreERT2/CreERT2}$* mice 6 weeks post-initiation with Ad-FlpO. (B) Long-term 3D cultures of primary mouse LUAD cells isolated from *BRaf$^{CA/+}$;Trp53$^{f/f}$;Nkx2-1$^{f/+}$;Rosa26$^{tdTomato/tdTomato}$* (BP) and *BRaf$^{CA/+}$;Trp53$^{f/f}$;Nkx2-1$^{f/f}$;Rosa26$^{tdTomato/tdTomato}$* (BPN) mice 8 weeks post-initiation. Shown are representative IHC photomicrographs. Scale bar: 100 μm.

Suppl FIG 4

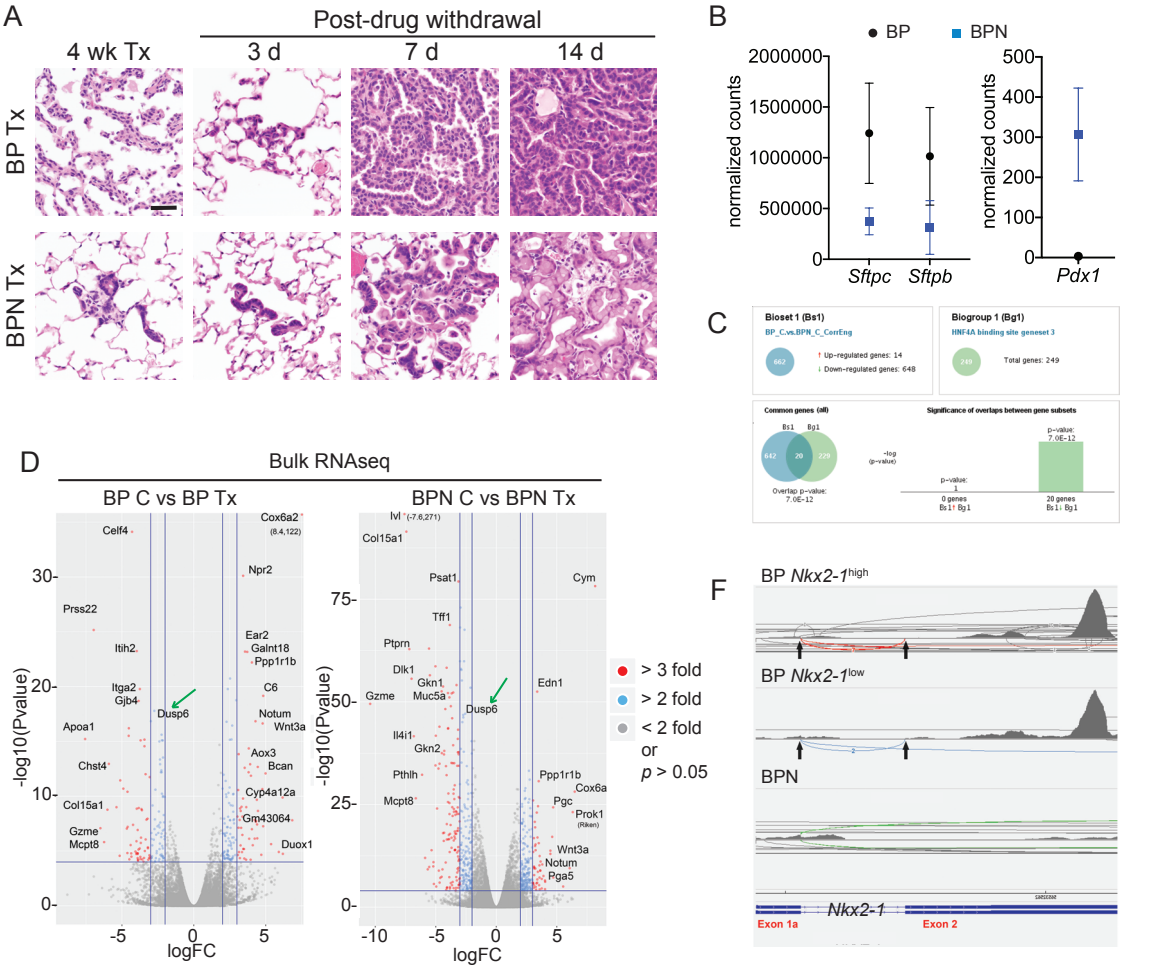
A
Post-drug withdrawal
4 wk Tx
3 d
7 d
14 d
BP Tx
BPN Tx
B
BP
BPN
normalized counts
Sftpc
Sftpb
Pdx1
C
D
Bulk RNAseq
BP C vs BP Tx
BPN C vs BPN Tx
-log10(Pvalue)
logFC
> 3 fold
> 2 fold
< 2 fold
or
p > 0.05
F
BP Nkx2-1high
BP Nkx2-1low
BPN
Nkx2-1
Exon 1a
Exon 2

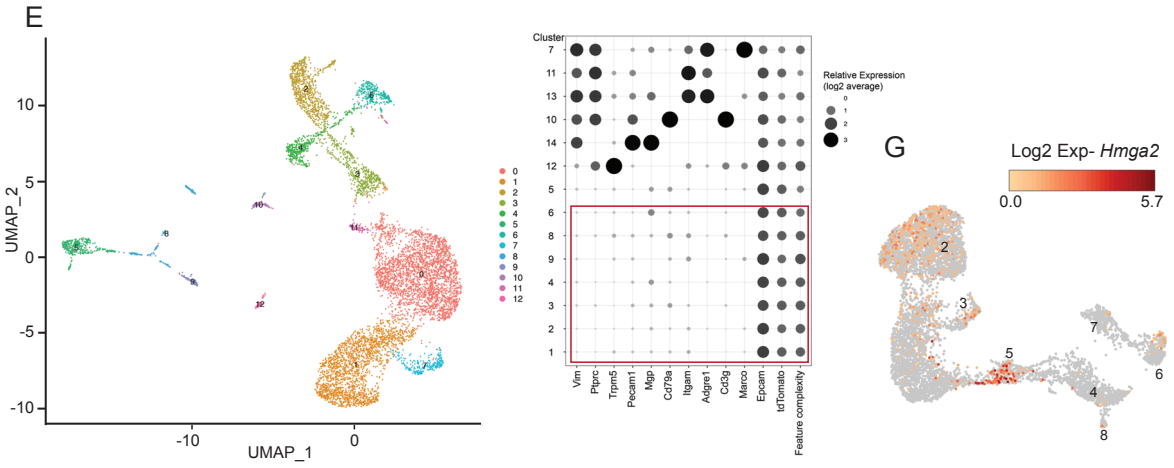
E
UMAP_1
UMAP_2
Cluster
Relative Expression
(log2 average)
Vim
Ptprc
Trpm5
Pecam1
Mgp
Cd79a
Itgam
Adgre1
Cd3g
Marco
Epcam
tdTomato
Feature complexity
G
Log2 Exp- Hmga2
0.0
5.7

Figure S4. NKX2-1 status modulates response to MAPK pathway inhibitors

(A) Representative histology of BP and BPN tumors after 4 weeks of combined $BRAF^{V600E}$ and MEK inhibitor chow treatment, as well as at different timepoints following drug withdrawal demonstrating rapid tumor relapse. (B) Graphs comparing absolute expression levels of direct NKX2-1 targets (*Sftpc* and *Sftpb*) as well as the gastrointestinal marker *Pdx1* in BP (n=8) and BPN (n=9) tumors, data obtained from bulk RNA sequencing. (C) Bulk RNAseq analyses of BP and BPN tumors via Illumina Correlation Engine indicating that HNF4α binding site geneset 3 becomes significantly enriched upon loss of *Nkx2-1*. (D) Volcano plots of bulk RNA sequencing data from control and MAPK inhibitor-treated BP tumors (left) and BPN tumors (right) indicating differentially expressed genes (EdgeR) (see also Supplementary Tables 2, 3). Select highly differentially expressed genes are highlighted. (E) Left- UMAP visualization of single cell transcriptome relatedness indicating 14 distinct clusters. Right- Relative expression of stromal marker genes and feature complexity score used in selecting high complexity tumor clusters that lack stromal marker gene expression for further analysis (red box). * Lower than average complexity. (F) Sashimi plots visualizing raw RNAseq densities along *Nkx2-1* exons and splice junction for *Nkx2-1*-positive and *Nkx2-1*-negative single tumor cells from their alignment data. Exon 1a-2 junctions and exon 2 reads are only detected in cells expressing *Nkx2-1* to variable degree indicating that these are incomplete recombinants (BP cells). (G) UMAP visualization of *Hmga2* expression in tumor clusters 1-8.

Suppl FIG 5

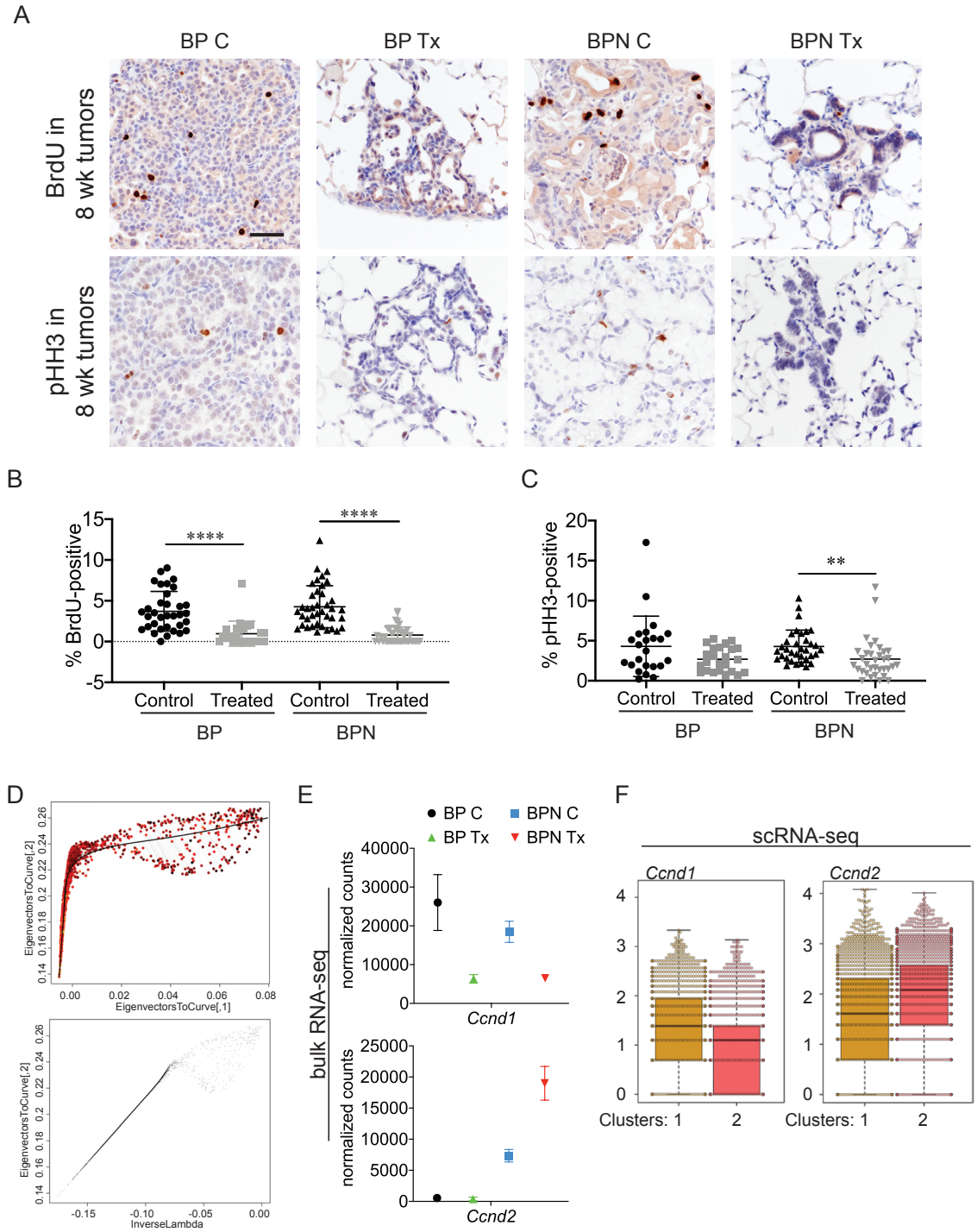
A
BP C
BP Tx
BPN C
BPN Tx
BrdU in 8 wk tumors
pHH3 in 8 wk tumors
B
% BrdU-positive
****
****
Control
Treated
Control
Treated
BP
BPN
C
% pHH3-positive
**
Control
Treated
Control
Treated
BP
BPN
D
EigenvectorsToCurve[,2]
EigenvectorsToCurve[,1]
InverseLambda
E
BP C
BPN C
BP Tx
BPN Tx
bulk RNA-seq
normalized counts
Ccnd1
Ccnd2
F
scRNA-seq
Ccnd1
Ccnd2
Clusters: 1
2
Clusters: 1
2

Figure S5. Differential impact of MAPK inhibitors on the cell cycle in NKX2-1$^+$ and NKX2-1$^-$ tumors

(A) Detection of proliferation markers, BrdU incorporation and phospho-histone H3 Ser10, by IHCs in neoplasia arising 8 weeks after tumor initiation with PGK-Cre lentivirus ($5x10^3$ pfu/mouse). At the 6 week timepoint, BP and BPN mice were given control or PLX4720 plus PD0325901 inhibitor chow for 2 weeks. Scale bar: 100 μm. (B) Quantification of BrdU-positive tumor cells from mice treated as in (A). Graphs represent mean ± S.D. BP C (34 tumors from 3 mice), BP Tx (23 tumors from 3 mice), BPN C (39 tumors from 3 mice), BPN Tx (40 tumors from 3 mice) were analyzed. ****$P < 0.0001$. (C) Quantification of phospho-HH3-positive tumor cells from mice treated as in (A). Graphs represent mean ± S.D. BP C (23 tumors from 2 mice), BP Tx (24 tumors from 2 mice), BPN C (34 tumors from 2 mice), BPN Tx (34 tumors from 2 mice) were analyzed. **$P = 0.0058$. (D) Figures showing how the trajectory for Q-depth was set. Top is a flattened version of the diffusion map based on arithmetic combination of the first three diffusion components with a principal curve to the resulting two dimensional graph and bottom plot is a pseudotime trajectory based on lambda values of the principal curve referred to here as Quiescence depth and shown on the x-axis. (E) Graph comparing absolute expression levels of *Ccnd1* and *Ccnd2*, data obtained from bulk RNA sequencing. (F) Relative abundance of *Ccnd1* and *Ccnd2* transcripts in scRNA-seq data on a cell-by-cell basis for clusters 1 and 2.

Suppl FIG 6

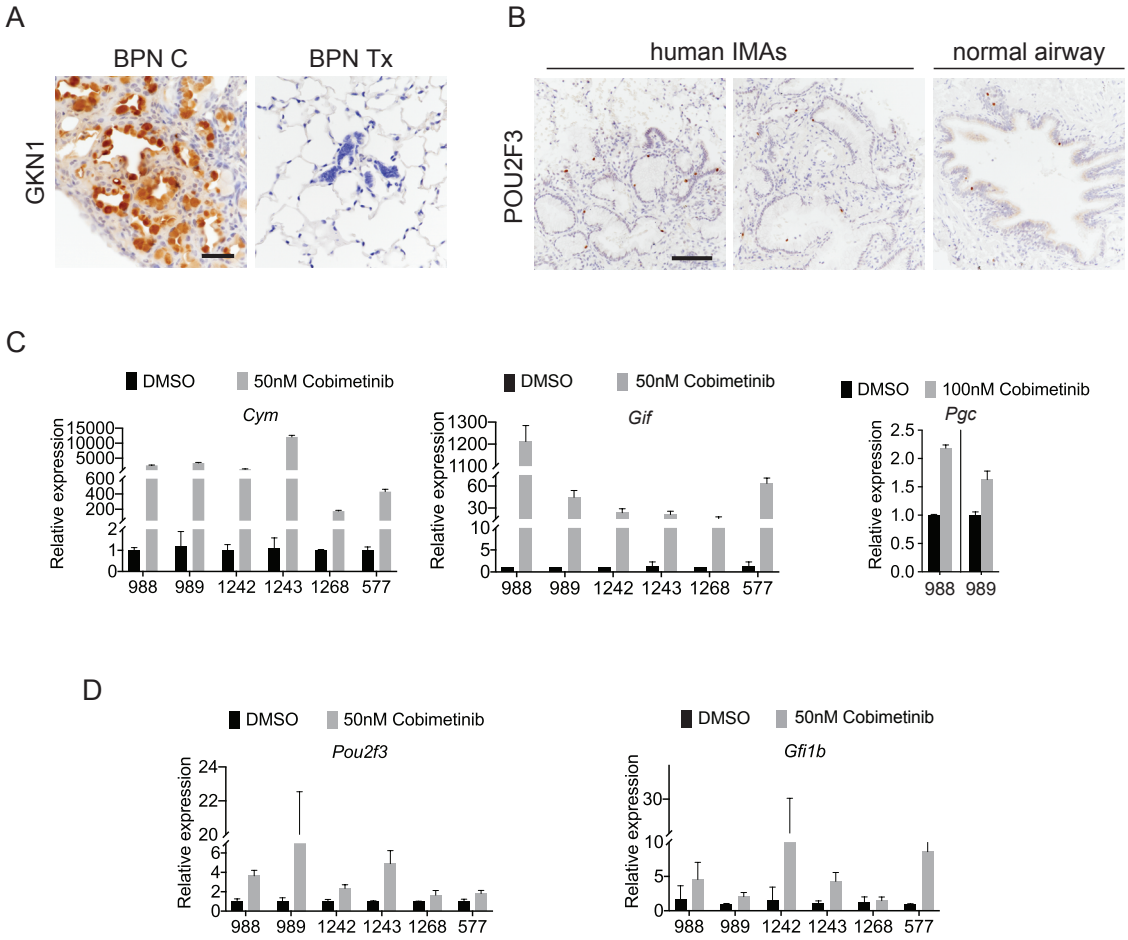
A
BPN C
BPN Tx
GKN1
B
human IMAs
normal airway
POU2F3
C
DMSO
50nM Cobimetinib
Cym
Relative expression
988 989 1242 1243 1268 577
DMSO
50nM Cobimetinib
Gif
Relative expression
988 989 1242 1243 1268 577
DMSO
100nM Cobimetinib
Pgc
Relative expression
988 989
D
DMSO
50nM Cobimetinib
Pou2f3
Relative expression
988 989 1242 1243 1268 577
DMSO
50nM Cobimetinib
Gfi1b
Relative expression
988 989 1242 1243 1268 577

Figure S6. MAPK activity regulates cellular identity in NKX2-1-negative tumors

A) IHC for detection of the surface neck mucous marker, GKN1, in control BPNs and BPN tumors that were treated with drug chow for 2 weeks. Scale bar: 100 μm. (B) IHC for the tuft cell marker, POU2F3, in two human IMAs (left, center) and normal airway epithelium (right). Scale bar: 100 μm. (C, D) qRT-PCR determination of the expression levels of select stomach epithelium lineage markers in multiple lung tumor organoid lines. Spheroid cultures were established from *BRaf*$^{CA/+}$*;Trp53*$^{f/f}$*;Nkx2-1*$^{f/f}$*;Rosa26*$^{tdTomato/tdTomato}$ mice (for BPN lines: 988, 989, 1242 and 1243), or for the KPN lines from *KRas*$^{LSL-G12D/+}$*;Trp53*$^{f/f}$*;Nkx2-1*$^{f/f}$*;Rosa26*$^{tdTomato/tdTomato}$ mice (for 1268), and from tamoxifen treated *KRas*$^{frtSfrt-G12D/+}$*;Trp53*$^{frt/frt}$*;Nkx2-1*$^{f/f}$*;Rosa26*$^{CreERT2/CreERT2}$ mice (for 577). Spheroids were subsequently cultured long term in 50% L-WRN conditioned media. For experiments, organoids were passaged (day 0) and allowed to recover overnight in the absence of DMSO/inhibitors. In each case, data are presented as fold change (mean±S.D.) compared with DMSO control values. (C, D) RNA derived from indicated BPN and KPN organoid lines that had been treated with DMSO or Cobimetinib for 72 hours. (C) qRT-PCR for detection of markers of gastric gland base cell types. (D) qRT-PCR for detection of tuft cell-specific transcripts. Data shown for each marker are representative of 2 or 3 independent experiments. Graphs represent mean ± S.D.

Suppl FIG 7

A

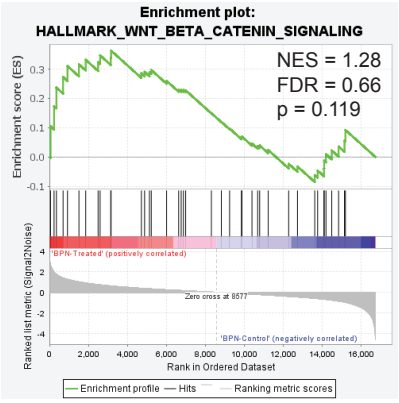

B

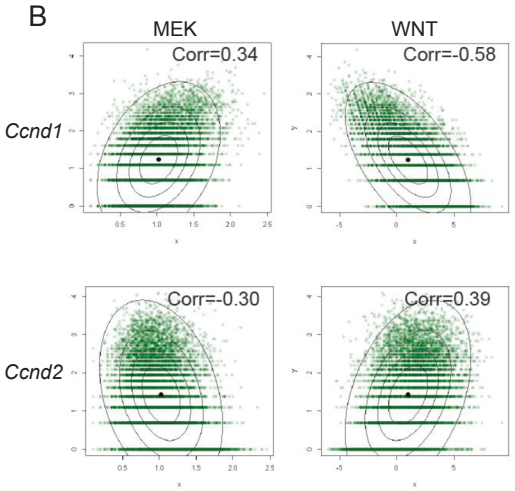

C

KEY
a = 50% LWRN + DMSO
b = 50% LWRN + 50nM Cobimetinib
c = 5% LWRN + DMSO
d = 5% LWRN + 50nM Cobimetinib
e = 5% LWRN + 200nM LGK-974
f = 5% LWRN + 200nM LGK-974
+ 50nM Cobimetinib

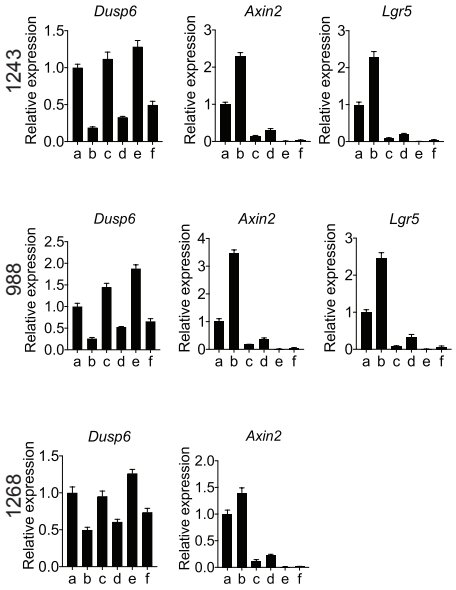

D

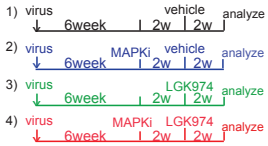

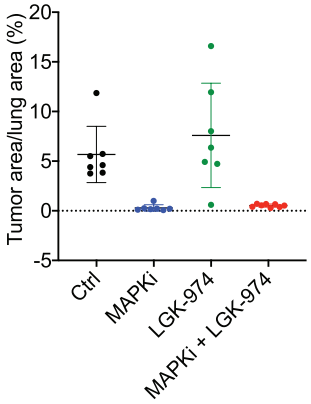

E

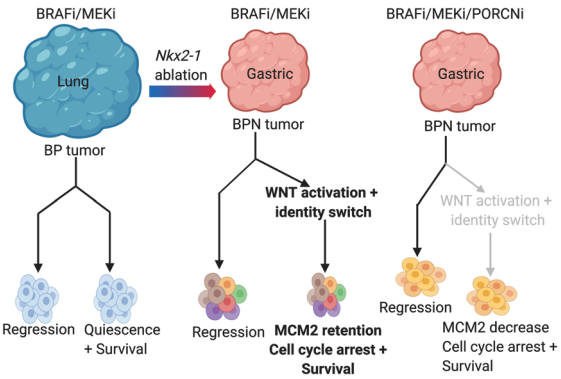

Figure S7. Shift in cellular identity renders BPN cells susceptible to Porcupine inhibitor.

(A) Enrichment plot for genes associated with canonical WNT activation in BPN treated versus control cells- data from bulk RNAseq. NES, Normalized Enrichment Score; FDR, False Discovery Rate. (B) Density plots and correlation values for a MEK activation signature (x-axis left two panels) and a WNT signature (x-axis right two panels) versus *Ccnd1* and *Ccnd2* transcript levels as indicated based on scRNA-seq. (C) Analyses of indicated gene expression levels in BPN (1243 and 988) and KPN (1268) tumor organoid lines by qRT-PCR at 24 hours and under different treatment conditions. Organoids were cultured in 50% L-WRN (a, b) or reduced 5% L-WRN media (c, d, e, f) and treated with DMSO (a, c), single agent Cobimetinib (b, d) or the Porcupine inhibitor, LGK-974 (e), and both inhibitors (f). Graphs indicate mean±S.D. Experiment was reproducibly performed 3 times. (D) Quantitation of lung tumor burden 10 weeks post-initiation in BPN mice under four different treatment conditions: 1) control (n=7); 2) MAPK-inhibitor chow (n=7); 3) LGK-974 (n=7); and 4) MAPK-inhibitor chow and LGK-974 (n=8). (E) Graphical depiction of the molecular and pharmacological regulation of differentiation programs in LUAD.